Electromagnetic Impact from Electric Propulsion on Aircraft

In collaboration with Heart Aerospace AB

Master's thesis in Sustainable Electric Power Engineering and Electromobility

BHARATHI SUBRAMANIAM MUTHURAMALINGAM

ROSHAN THOMAS

DEPARTMENT OF ELECTRICAL ENGINEERING

CHALMERS UNIVERSITY OF TECHNOLOGY
Gothenburg, Sweden 2024
www.chalmers.se

Master's thesis 2024

Electromagnetic Impact from Electric Propulsion on Aircraft

In collaboration with Heart Aerospace AB

BHARATHI SUBRAMANIAM MUTHURAMALINGAM
ROSHAN THOMAS

Department of Electrical Engineering
Division of Electric Power Engineering
Chalmers University of Technology
Gothenburg, Sweden 2024

Electromagnetic Impact from Electric Propulsion on Aircraft
In collaboration with Heart Aerospace AB
BHARATHI SUBRAMANIAM MUTHURAMALINGAM
ROSHAN THOMAS

Supervisor: Johan Hellsing, Heart Aerospace AB
Examiner: Torbjörn Thiringer, Electric Power Engineering

Master's Thesis 2024
Department of Electrical Engineering
Division of Electric Power Engineering
Chalmers University of Technology
SE-412 96 Gothenburg
Telephone +46 31 772 1000

Cover: Picture of the ES-30 Copyright. Heart Aerospace 2024 [1]

Typeset in LaTeX
Printed by Chalmers Reproservice
Gothenburg, Sweden 2024

Electromagnetic Impact from Electric Propulsion on Aircraft
In collaboration with Heart Aerospace AB
BHARATHI SUBRAMANIAM MUTHURAMALINGAM & ROSHAN THOMAS
Department of Electrical Engineering
Chalmers University of Technology

Abstract

This thesis investigates the Conducted Electro Magnetic Interference (EMI) characteristics of Direct Current (DC) power cables in electric aircraft systems, focusing on the behaviour of unshielded and shielded cables across a frequency range of 1 Hz to 10 MHz. The DC ripple current flowing from the battery to the inverter is modeled and quantified using Simulink. This ripple current is fed to the cable model in COMSOL for analysis of cross-talk with a neighbouring cable. The study examines the impact of DC ripple currents and induced voltage in neighbouring cables due to electromagnetic coupling.

Key findings include the calculation of the DC ripple current in the unshielded and shielded cases. Peak-Peak ripple of 140 A was seen in the unshielded cable and 230 A in the shielded case. Higher DC ripple currents are due to the complex interactions of induced currents within the shielding layer. These findings emphasize the critical need for considering high-frequency EMI effects in designing the DC power cable systems to ensure optimal performance and regulatory compliance. The cables exhibited significant conducted EMI at the inverter's switching frequency of 25 kHz, reaching approximately 160 dBμA. The effectiveness of shielding and distance between the cables was studied by analyzing the effect on the victim cable placed 100 mm above the cable. Analysis indicated that the induced voltage was reduced in the victim cables as the power cables were brought closer to each other. Finally, the study indicated that the amount of induced voltage is reduced when shielded cables are used.

Future work should involve practical testing to validate these simulation results and explore further mitigation strategies for both conducted and radiated emissions in electric aviation applications.

Keywords: EMI, DC power cables, conducted emissions, shielding effectiveness, COMSOL, DC ripple current, electric aircraft systems.

Acknowledgements

This work has been carried out at the Department of Electrical Engineering at Chalmers University of Technology. We extend our sincere gratitude to Johan Hellsing, our supervisor at Heart Aerospace, for his exceptional support and guidance. His invaluable insights and constructive feedback have been crucial in shaping this thesis. We deeply appreciate his patience, understanding, and commitment, which have greatly contributed to the successful completion of this research.

We would also like to extend our sincere gratitude to our examiner at Chalmers, Professor Torbjörn Thiringer, for his thoughtful evaluation and valuable feedback, which have greatly enhanced the quality of this thesis.

We also thank Hannes Pfitzner and Bichoi Wael at Heart Aerospace for their assistance with our thesis.

Last but certainly not least, we owe our deepest gratitude to our families. Their unwavering support and standing by us through every high and low have been our source of strength and inspiration.

Bharathi Subramaniam Muthuramalingam
Roshan Thomas

Gothenburg, August 2024

List of Acronyms

Below is the list of acronyms that have been used throughout this thesis listed in alphabetical order:

CE	Conducted Emissions
CISPR	Comité International Spécial des Perturbations Radioélectriques
DC	Direct Current
DM	Differential Mode
DPWM	Discontinous Pulse Width Modulation
EECM	Equivalent Electrical Circuit Model
EESI	Environmental and Energy Study Institute
EIS	Electrochemical Impedance Spectroscopy
EMC	Electro Magnetic Compatibility
EMF	Electro Magnetic Field
EMI	Electro Magnetic Interference
ESR	Equivalent Series Resistance
FAA	Federal Aviation Administration
FCC	Federal Communications Commission
FFT	Fast Fourier Transform
HV	High Voltage
IGBT	Insulated Gate Bipolar Transistor
LD	Lorentz-Drude
NASA	National Aeronautical Space Agency
OCV	Open Circuit Voltage
PDU	Power Distribution Unit
PMSM	Permanant Magnet Synchronous Machine
PWM	Pulse Width Modulation
RE	Radiated Emissions
RTCA	Radio Technical Commission for Aeronautics
SOC	State of Charge
SPWM	Sinusoidal Pulse Width Modulation
SVPWM	Space Vector Pulse Width Modulation
XLPE	Cross Linked Polyethylene

Nomenclature

Below is the nomenclature of variables that have been used throughout this thesis.

Variables

R	Resistance
C	Capacitance
R_{int}	Internal resistance of battery
H	Magnetic Field Strength
I	Amplitude of the reference current
J	Current density vector
E	Electric field vector
ρ_v	Volume charge density
μ	Magnetic permeability
W_e	Electric Energy
W_m	Magnetic Energy
r_c	Resistance of conductor
r_s	Resistance of shield
l_c	Self-inductance of conductor
l_s	Self-inductance of shield
c_c	Shunt capacitance of cable
M_{c1s1}	Mutual inductance between conductor 1 & shield 1
M_{c1s2}	Mutual inductance between conductor 1 & shield 2
ϵ_r	Complex dielectric permittivity
ω_p	plasma frequency

Contents

List of Acronyms ix

Nomenclature xi

1 Introduction 1
- 1.1 Problem Background 1
- 1.2 Purpose Statement 2
- 1.3 Scope and Limitations 2
- 1.4 Ethics 3

2 Theory 5
- 2.1 Battery Modeling 5
  - 2.1.1 R_{int} model 5
  - 2.1.2 RC model 6
- 2.2 Cable Modeling 7
  - 2.2.1 Lorentz-Drude model 7
  - 2.2.2 Calculation of frequency-dependent parameters 8
  - 2.2.3 Skin effect 9
- 2.3 Conducted EMI 9

3 Case set-up 13
- 3.1 Setup for study 13
- 3.2 Measurements 13
- 3.3 Simulink model 14
  - 3.3.1 Battery Modeling 14
  - 3.3.2 Cable Modeling 17
    - 3.3.2.1 Unshielded Cable 17
    - 3.3.2.2 Shielded Cable 18
  - 3.3.3 Inverter Modeling 19
  - 3.3.4 Motor Modeling 20
- 3.4 COMSOL model 21
  - 3.4.1 Cable modeling for parametrization 21
    - 3.4.1.1 Unshielded cable 21
    - 3.4.1.2 Shielded cable 22
  - 3.4.2 Modeling of the Cable for Parametric Distance Sweep 23

4 Analysis 25

4.1 Frequency dependent parameters 25
  4.1.1 Resistance 25
  4.1.2 Inductance 27
4.2 Analysis of DC Ripple current and DC Voltage ripple 30
4.3 Analysis of Equivalent Series Resistance (ESR) in DC Link Capacitor 35
4.4 Analysis of induced voltage in the victim cable 37

5 Conclusions 41
5.1 Results 41
5.2 Future work 41

Bibliography 43

A Appendix 1 I
A.1 Parameters for cable modelling I

1

Introduction

1.1 Problem Background

The aviation industry plays an important role in the global economy, enabling passenger and freight transport, and is currently experiencing significant growth. The Federal Aviation Administration (FAA) indicated that passenger levels for commercial air travel in the U.S. rose by 4.2% during the last financial year before the COVID-19 pandemic. Projections suggest that this growth trend will persist, with total air traffic operations at control towers anticipated to escalate from 53 million in 2019 to nearly 64 million by 2040, underscoring a sustained increase in air travel demand [2]. The Environmental and Energy Study Institute (EESI) report highlights that aviation significantly contributes to greenhouse gas emissions, with the majority of these emissions occurring at altitudes above 3,000 feet, impacting both global and local air quality. Additionally, the ground operations of aircraft and airport service vehicles worsen local pollution by emitting nitrogen oxides, sulfur oxides, hydrocarbons, and particulate matter [3].

The development of electric aircraft offers a promising solution to traditional aircraft design and has attracted significant attention from various companies. One of its most significant advantages is its potential to address environmental concerns. Despite the unique set of challenges it poses, the design of electric aircraft presents a unique set of challenges. One notable issue is the limited energy density of batteries, which currently restricts electric aircraft to short flights. However, with ongoing research and development, this limitation is expected to be overcome, paving the way for a more sustainable future of aviation.

One of the novelties of electric aviation is the introduction of high-voltage inverters. To ensure a safe and functional aircraft, it must be assured that the electromagnetic emissions of the inverters do not affect itself and other systems of the aircraft. Typically, the systems on the aircraft are qualified to comply with certain levels of electromagnetic emissions; however, today's standards do not cover emissions from the inverter.

One of the few examples is the electric aircraft developed by National Aeronautical Space Agency (NASA). The NASA X-57 Maxwell project encountered significant challenges related to EMI. EMI issues primarily arose due to the high-power electric propulsion systems and the distributed nature of the electric motors along the wings [4].

DO-160, a standard for environmental conditions and test procedures for airborne equipment given by Radio Technical Commission for Aeronautics (RTCA), does not fully address the specific EMI requirements for 800V inverters used in electric aircraft. The existing standards primarily focus on general aviation equipment and their interaction with traditional aircraft electrical systems. However, the unique high-voltage and high-frequency switching characteristics of 800V inverters present additional challenges in EMI control that are not comprehensively covered by DO-160 [5].

For instance, the standard lacks specific guidelines for managing the high-frequency switching noise and the potential for increased EMI emissions from such high-power systems. These issues necessitate enhanced shielding, grounding techniques, and tailored EMI filters that go beyond what DO-160 currently mandates. This gap requires additional testing and mitigation strategies to ensure the safe and reliable operation of high-voltage electric propulsion systems in aircraft.

1.2 Purpose Statement

This project aims to investigate the electromagnetic emissions produced by the power electronic system of an electric aircraft. The knowledge about emissions from these high voltage systems is not quite well known. The study will analyse the ripple current from the battery to the inverter over a wide frequency range. The first step of the study involves creating a battery model and then moving on to cable modelling, including shielded and unshielded cables. These cables will be modelled using the equivalent circuit method in Simulink. The load under analysis is a three-phase inverter, which will also be modelled using Simulink. The DC ripple current from the battery to the inverter will be modelled and quantified using Simulink. Finally, the Electro Magnetic Field (EMF) from the cables will be calculated using COMSOL software. This software analyses the EMF radiated from the cables. The fields interacting with the interconnecting cables that run near the power cables are also studied and analysed.

1.3 Scope and Limitations

This thesis provides an in-depth examination of the EMI characteristics of DC power cables within electric aircraft systems, a novel study area due to the emerging nature of electric aviation. Specifically, the research quantifies the EMI present in unshielded and shielded cables, analysing their behaviour across a frequency range from 1 Hz to 10 MHz. The study highlights the potential impacts on nearby cables and overall system performance by delving into the interactions between EMI and other connected loads, such as DC-DC converters. This exploration addresses the unique challenges of high-voltage, high-frequency switching in electric propulsion systems. It bridges a critical gap in the existing literature by merging insights from power electronics and high-voltage engineering.

Several factors constrain the research. Firstly, the experimental measurements are confined to specific cable configurations and may not capture all possible variations encountered in real-world scenarios. Additionally, the study relies solely on simulations, without practical testing of EMI. Although simulations offer valuable insights, they cannot fully replicate the conditions and complexities of real-world environments and struggle to replicate complex electromagnetic interactions, such as the behavior of waves around physical obstructions and material properties, which are critical for precise measurements. External factors, such as electromagnetic interference from other sources and varying environmental conditions, are not controlled and might affect the results. Also, the focus of this thesis is limited to Conducted Emissions (CE) and does not encompass Radiated Emissions (RE). Simulating radiated emissions accurately is challenging for the reasons mentioned above.

Assumptions regarding material properties and environmental conditions could influence the findings, and the COMSOL models, despite their detail, cannot ideally mimic the complex interactions present in practical applications.

1.4 Ethics

This study upholds strict ethical standards, ensuring accurate data management and analysis according to relevant regulations. Focused on simulations, the research avoids involving human participants and prioritises integrity and responsible data handling. All sources are properly cited, and licensed software is used in compliance with agreements. Sensitive information and intellectual property from Heart Aerospace are handled with care, maintaining integrity throughout.

While the study does not directly address environmental or societal impacts, it recognizes the importance of EMI on electronic device safety. The findings contribute to the development of safer, more efficient electric power systems and align with the UN's goal of reducing CO_2 emissions in electric aviation. The research complies with ethical guidelines from Chalmers University of Technology and international standards, with full transparency and disclosure of any potential conflicts of interest, and it addresses societal, ethical, and ecological considerations as recommended by the university.

2

Theory

2.1 Battery Modeling

Battery modeling plays an important role in this project as a correct representation of the model is needed to simulate the propulsion system designed by Heart Aerospace. Battery models are essential for accurately simulating and predicting battery performance, efficiency, and lifespan across various applications. They help in comprehending internal dynamics like the voltage, current, and temperature behaviours, which are critical for designing effective Battery Management Systems and accurate quantification of the CE.

Various battery models are available, ranging from basic to highly sophisticated. Initially, a simple model was employed, and complexity was progressively incorporated to develop the final version. For example, starting with the R_{int} model, which includes an ideal voltage source and series resistance, the approach then moved to the Thevenin model, which adds RC (resistor-capacitor) networks to better capture dynamic behaviours. Ultimately, an advanced equivalent circuit model was adopted, accounting for State of Charge (SOC), state of health, and temperature effects to provide a comprehensive representation of the battery's performance under varying conditions.

2.1.1 R_{int} model

The R_{int} model, often termed the resistive model, simplifies a battery's representation by combining an ideal voltage source with a series resistor. The voltage source reflects the battery's Open Circuit Voltage (OCV), which fluctuates based on the SOC.

The series resistor accounts for the internal resistance, causing voltage drops when the current flows. This model's simplicity is beneficial for basic simulations, but it lacks the capacity to simulate dynamic behaviours like transient responses and temperature variations, thus limiting its accuracy for more complex scenarios [6]. A model representation is shown in Figure 2.1.

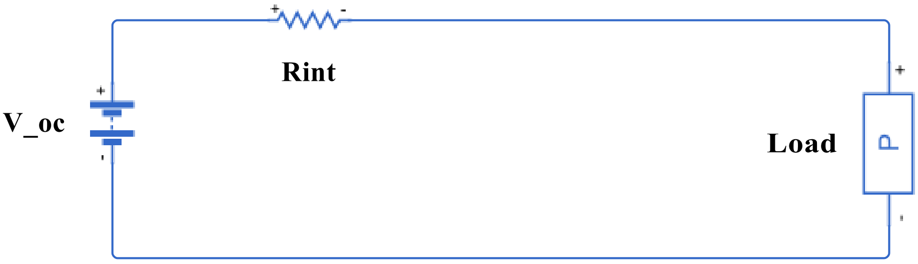

Figure 2.1: Simple R_{int} model

2.1.2 *RC* model

RC (Resistor-Capacitor) networks as depicted in Figure 2.2 are fundamental components in the electrical modelling of batteries. They are used to replicate the dynamic response of batteries to various load conditions. The *RC* model consists of a resistor and capacitor in parallel, representing the battery's internal resistance and capacitance. These networks help simulate both the instantaneous voltage drop and the slower diffusion processes occurring within the battery, providing a more comprehensive understanding of battery behaviour during charging and discharging cycles. By capturing these dynamics, *RC* models enable more accurate predictions of battery performance and lifespan.

The basic structure of an *RC* model includes a voltage source representing the OCV of the battery, in series with an ohmic resistance (R_{int}), which models the internal resistance of the battery. This is followed by one or more *RC* pairs. Each *RC* pair consists of a resistor and a capacitor in parallel, which together model the transient behaviors and interfacial charge-transfer reactions at the electrodes. In a first-order *RC* model, a single *RC* pair is used, which captures essential dynamic behaviors but may lack the precision required for more complex scenarios. For greater accuracy, second-order or higher-order *RC* models can be employed, adding additional *RC* pairs to better simulate the battery's transient responses and internal diffusion processes. Additionally, an extra parallel resistance R_L can be added alongside the series inductance L_R to model the inductive behavior at high frequencies.

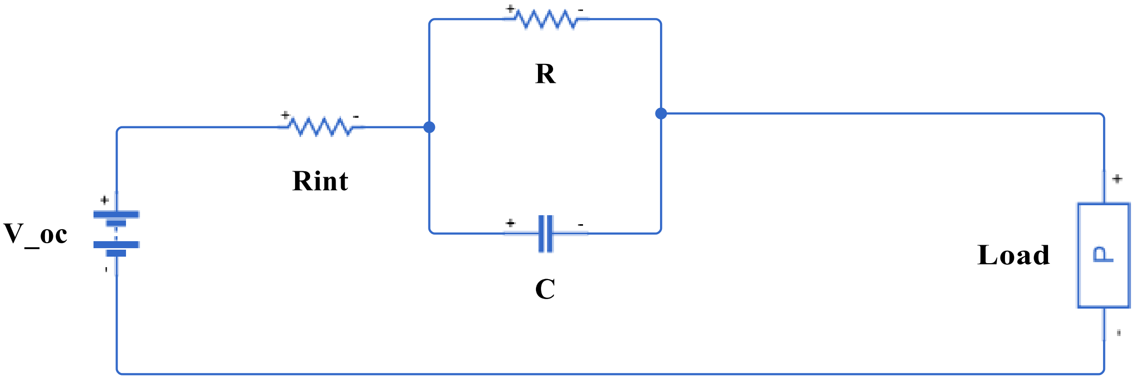

Figure 2.2: *RC* battery model

The overall battery cell impedance of an RC-element model [7] including n RC-elements can be described as

$$\bar{Z}_{\text{Cell,RC}} = j\omega L_R + R_0 + \sum_{i=1}^{n} \frac{R_i}{1 + j\omega R_i C_i}. \tag{2.1}$$

These RC networks are parameterized using techniques such as Electrochemical Impedance Spectroscopy (EIS) [7]. EIS measures the impedance of the battery over a wide range of frequencies, providing data that can be used to determine the values of the resistors and capacitors in the RC network. By fitting the model parameters to the EIS data, the RC model can accurately reflect the battery's behavior under different operating conditions.

2.2 Cable Modeling

Research indicates that EMI can originate from the DC cables connecting the battery and inverter, affecting system performance and Electro Magnetic Compatibility (EMC) compliance. Specifically, common-mode currents in DC cables can act as antennas, radiating EMI that interfere with other electronic components in electric vehicles [8]. This highlights the importance of thorough EMI analysis and mitigation in battery-inverter systems. Shielded and unshielded cables are analysed in this study. Shielded cables effectively enhance EMC and help meet EMI compliance and regulatory standards, making them ideal for high-frequency power electronic systems prone to significant EMI propagation through cables. The degree of EMI protection can be varied based on the shielding level of the cable, categorized into braided cables that account for 90% shielding, spiral cables that correspond to 98% shielding, and metal-coated mylar or foil cables for 100 % shielding. In contrast, unshielded cables, consisting only of the conductor, are more susceptible to external interference.

2.2.1 Lorentz-Drude model

The Lorentz-Drude (LD) model is crucial for accurately modeling the electromagnetic properties of cables, particularly in predicting impedance and frequency-dependent behaviour. The LD model expands upon the Drude model by including both the behaviour of free electrons and the response of polarizable materials. In this model, polarizable matter is represented by harmonic oscillators, simulating various microscopic processes such as electron transitions and lattice vibrations [9].

The complex dielectric permittivity function $\hat{\epsilon}_r(\omega)$ in the LD model is expressed as the sum of two components [10]

$$\hat{\epsilon}_r(\omega) = \hat{\epsilon}_r^{(f)}(\omega) + \hat{\epsilon}_r^{(b)}(\omega) \tag{2.2}$$

The first component, $\hat{\epsilon}_r^{(f)}(\omega)$, represents intraband effects related to free electrons, and is given by the Drude model

$$\hat{\epsilon}_r^{(f)}(\omega) = 1 - \frac{\omega_p^2}{\omega(\omega - i\Gamma_0)}, \tag{2.3}$$

where ω_p is the plasma frequency and Γ_0 is the damping constant.
The second component, $\hat{\epsilon}_r^{(b)}(\omega)$, accounts for interband effects involving bound electrons, and is modelled similarly to the Lorentz model for insulators

$$\hat{\epsilon}_r^{(b)}(\omega) = \sum_{j=1}^{k} \frac{f_j \omega_p^2}{\omega_j^2 - \omega^2 + i\omega\Gamma_j}, \tag{2.4}$$

Here, k is the number of oscillators, each with its specific frequency ω_j, strength f_j, and damping constant Γ_j [11].

The motion of these harmonic oscillators in the LD model is described by the equation of motion for two oppositely charged particles connected by a spring, driven by an external electric field oscillating with frequency ω. The LD model effectively combines the dynamics of free and bound electrons, offering a comprehensive framework for understanding the optical properties of metals and other materials.

2.2.2 Calculation of frequency-dependent parameters

The calculation of frequency-dependent parameters is explained in this section. The resistance, inductance, and capacitance of both unshielded and shielded cables are shown based on research provided by COMSOL software [12].

The electric energy stored in the electric field for volume charges can be calculated by

$$W_e = \frac{1}{2} \iiint \rho_v V dv \tag{2.5}$$

It shows that the energy stored in the electric field (W_e) is directly proportional to the volume charge density (ρ_v) and also the electric potential.

From (2.5), we can calculate the capacitance

$$C = \frac{2W_e}{V^2} \tag{2.6}$$

Here, C is the capacitance, and V is the potential applied.

The equation to calculate the energy stored in the magnetic field W_m is

$$W_m = \frac{1}{2} \iiint \mu H^2 dV \tag{2.7}$$

Here H is the magnetic field strength and μ is the permeability of the material.

The inductance can be calculated by

$$L = \frac{2W_m}{I^2} \tag{2.8}$$

Here L is the inductance and I is current through the coil.

Resistance is calculated as

$$R = \frac{1}{|I|^2} \iint \mathbf{J}^* \cdot \mathbf{E} dS \tag{2.9}$$

where R is the resistance, I is the amplitude of the reference current, J is the current density vector, E is the electric field vector. The numerator corresponds to volumetric loss density.

For all the above parameters, an additional multiplication factor of 2 is used in the calculation when transitioning from a time-dependent solution to the frequency domain as suggested by the COMSOL software.

2.2.3 Skin effect

The skin effect, typically associated with alternating current (AC), also has implications for DC systems, particularly those with high ripple currents. In DC systems, the skin effect is negligible under pure DC conditions because the current distribution remains uniform throughout the conductor's cross-sectional area. However, when high ripple currents are superimposed on the DC current, the conductor experiences alternating current components at the ripple frequency, causing a redistribution of current towards the surface of the conductor. This phenomenon leads to increased effective resistance as the skin depth changes, similar to the behaviour observed in AC systems [13]. This is particularly significant in applications such as power electronics and electric propulsion systems where high-frequency switching introduces substantial ripple currents [14].

2.3 Conducted EMI

Conducted EMI refers to unwanted noise currents that travel along the conductive paths in electrical systems. These emissions typically fall within the frequency range of tens of kHz to several MHz and can adversely affect the performance of other electronic devices and systems connected to the same power network. Conducted emissions are a critical consideration in the design and operation of power electronics, particularly in systems like DC-AC converters and inverters used in various applications, including electric aviation. Understanding conducted EMI involves examining the generation and propagation of noise within electrical circuits. Key sources of conducted EMI include switching actions in power converters, parasitic capacitances, and inductances within the circuit layout. The noise generated can couple into power lines and other interconnected circuits, potentially causing malfunctions or degradation in performance [15].

Effective mitigation of conducted EMI requires thorough modelling and analysis of the noise sources and propagation paths. Techniques such as using EMI filters, optimizing circuit layouts, and employing differential-mode and common-mode noise separators are commonly used to reduce conducted emissions. The goal is to ensure compliance with regulatory standards and to maintain the integrity and reliability of the overall system [16].

In addition, various modeling and prediction techniques for differential mode conducted EMI are crucial in the context of three-phase Pulse Width Modulation (PWM) inverters. Accurate modelling of layout parasitics, such as the inductance and capacitance, is essential for predicting the EMI emitted from these systems. Optimization of the layout and the selection of appropriate filter components can significantly reduce the levels of conducted EMI [17].

The conducted emissions are measured in dBμA. A logarithmic scale, like dBμA, is beneficial for measuring conducted emissions because it compresses the wide range of emission magnitudes into a more manageable form, simplifying visualization and comparison. For example, a 20 dBμA difference equates to a tenfold change in current, which is more intuitive than large numerical differences. Additionally, dBμA is a standardized unit in EMC testing and compliance, endorsed by international standards and regulatory bodies such as Comité International Spécial des Perturbations Radioélectriques (CISPR) and the Federal Communications Commission (FCC). This standardization ensures consistent measurement and reporting across various devices and manufacturers. The calculation of dBμA is shown below. The current levels at various frequencies are measured and converted into dBμA using the formula

$$\mathrm{dB}\mu\mathrm{A} = 20\log_{10}\left(\frac{I}{1\mu\mathrm{A}}\right) \tag{2.10}$$

The DO-160 standards for power cables (Category Q under Section 21 of DO-160), which deal with the CE, are shown in Figure 2.3. Although these standards were developed based on traditional aircraft systems, they provide valuable guidance on the acceptable emission levels for ensuring safe aircraft operation.

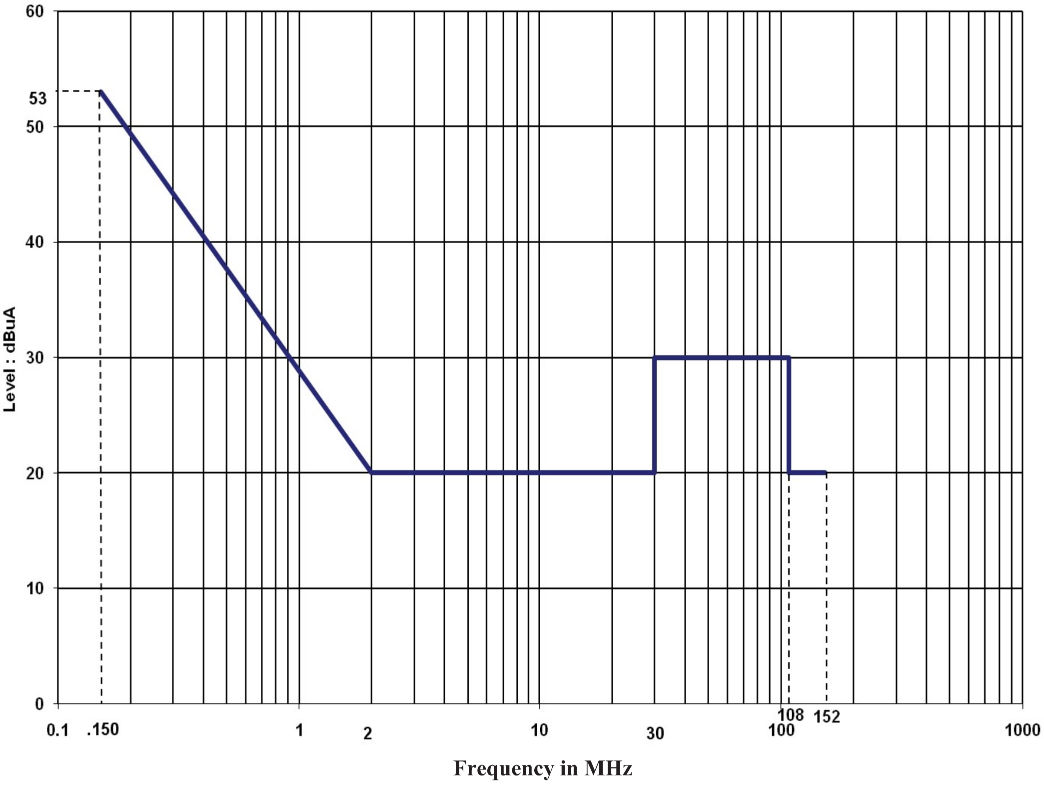

Figure 2.3: Maximum Level of CE Interference - Category Q Power Lines under DO-160, Section 21 [5]

3

Case set-up

3.1 Setup for study

The ES-30, a hybrid aircraft designed by Heart Aerospace and set to be commercialized in the upcoming years, features two electric propulsion units mounted in-board on the wing and two turboprop engines mounted out-board on the wing. The aircraft's electrical system is modeled in Simulink. The motor has a power rating of 1.6 MW, supplied by six three-phase inverters, with each inverter delivering 260 kW. The DC source for these inverters is provided by three battery packs, each with a capacity of 167 kWh, enabling each battery pack to power two inverters. The battery is connected to the Power Distribution Unit (PDU), which then connects to the inverter. Additionally, there are other 800 V system loads connected through the PDU. For the purpose of this project, the focus is on a single inverter supplying a 260 kW load. Consequently, the battery is designed with a capacity of 83.5 kWh. The system to be analysed is depicted in Figure 3.1.

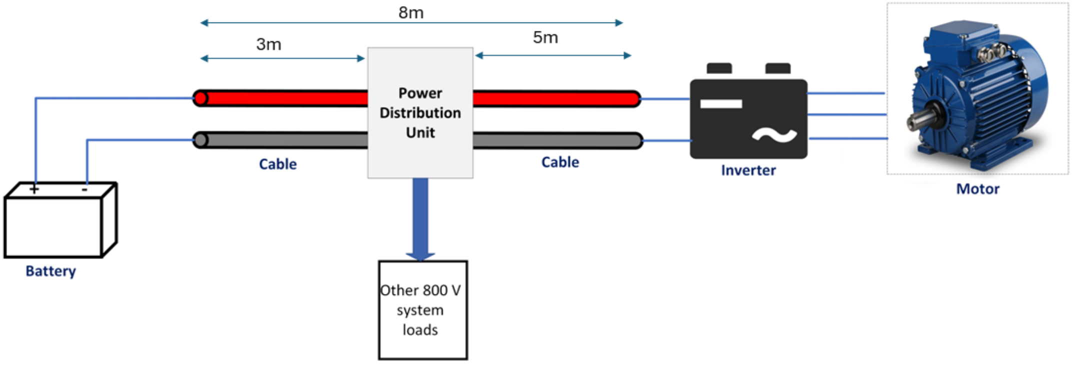

Figure 3.1: System to be analysed

3.2 Measurements

For measuring CE, the input ripple on the DC side needs to be determined. This involves setting up models for the battery, cable, and inverter using Simulink. The specific models for these components are detailed in subsequent sections. The DC ripple current is captured using Simulink's Current Sensor block. There are two primary methods to calculate CE: one involves feeding the current data into a Spectrum Analyzer block in Simulink, where the frequency range for the required analysis can be specified; the other method entails performing a manual Fast Fourier Transform (FFT). Both methods allow for the calculation of CE in decibel microamperes (dBμA).

The next focus is on cable modelling to analyze EMI from the cable, which falls within the scope of this thesis. The cable is modelled in COMSOL and subjected to the ripple current data obtained from Simulink. The setup in COMSOL will be detailed in the following section. Using the COMSOL model, the electric field around the cable is estimated, and the spacing between the two power cables is varied and analysed. Additionally, a victim cable, representing other electrical lines in the aircraft, is modelled to study the voltage induced in the victim cable due to the power cables' electromagnetic field.

3.3 Simulink model

The overall system designed in Simulink is depicted in Figure 3.2. This simulation setup includes configuring an appropriate sampling time, which determines the frequency range of the spectrum analyser according to the Nyquist criterion. The chosen sampling time for the simulation is 10 ns, enabling the analysis of frequencies up to 50 MHz. A fixed-step solver is employed for the simulation. The following sections detail the individual component modelling and their implementation in Simulink.

3.3.1 Battery Modeling

By aggregating the distributed dynamics of a battery, Equivalent Electrical Circuit Model (EECM) employ various electrical components, such as a voltage source, resistors, capacitors, and occasionally a non-linear element like Warburg impedance, to simulate battery behaviour [18]. The battery is modeled with a three RC network to more accurately simulate its dynamic response. The cell used for this study is the Samsung 30Q, as detailed in [7]. The parameters for the RC network are derived from this cell's data. A 6 Ah capacity cell with 231.25 Wh/kg specific energy is incorporated. The model includes a controlled voltage source, which receives inputs based on the battery's SOC. A lookup table is utilized to map the OCV of a single cell according to the system's SOC. This OCV is then multiplied by the number of series-connected cells to determine the OCV of the entire battery system. The instantaneous SOC is calculated using an integrator that takes current as input.

Additionally, two battery packs, each designed to provide 400 V, are connected in series to produce a total voltage of 800 V. This configuration allows the midpoint of the system to be grounded for simulation in MATLAB. The battery packs, each consisting of 20 parallel cells and 76 series cells, are connected in series to achieve the desired voltage nominal voltage of 700 V. In the battery model, an inductor is included to model the high-frequency response more accurately. The battery model representation is illustrated in Figure 3.3 and the EECM of the battery with the values is shown in Figure 3.4.

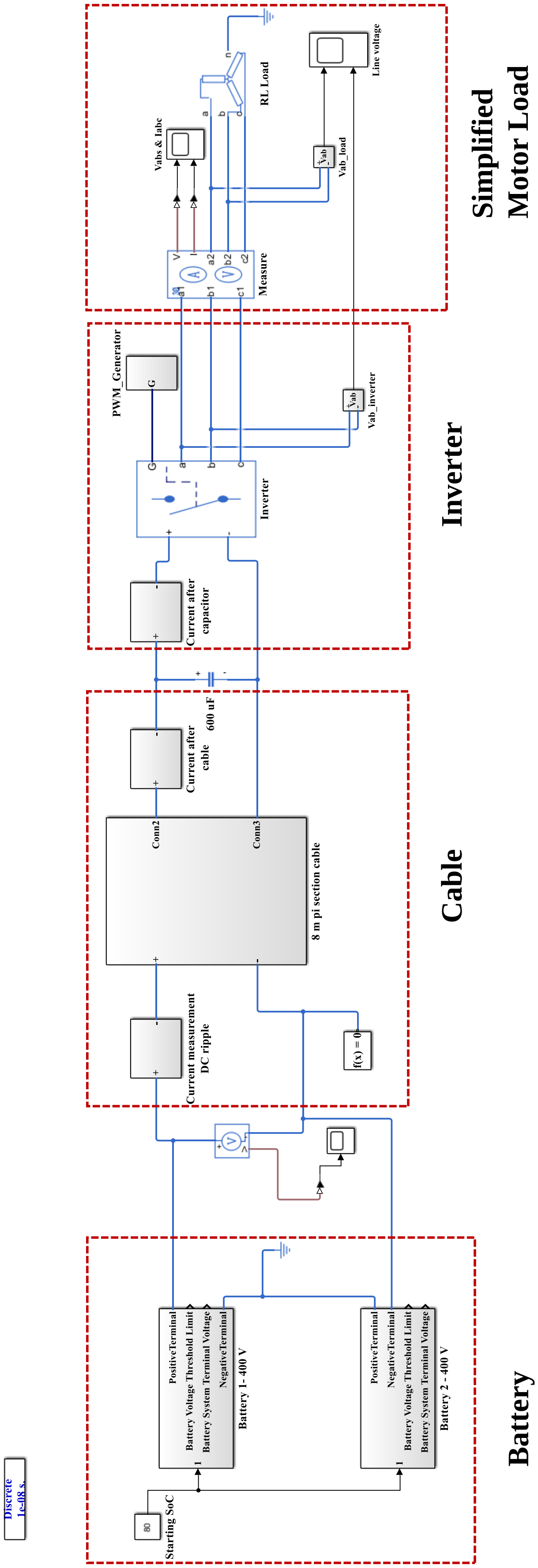

Figure 3.2: Simulink model of 260kW system to quantify the dc ripple current

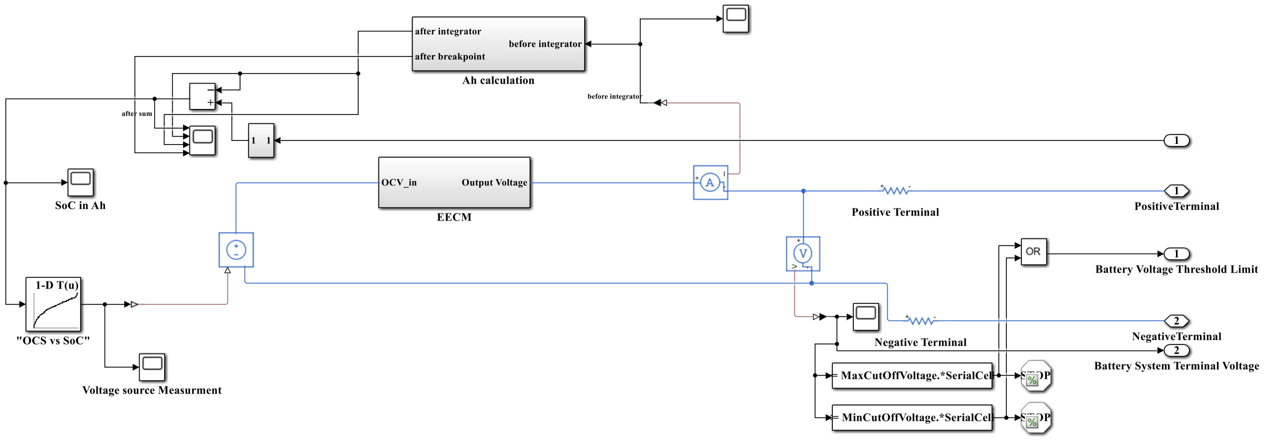

Figure 3.3: Simulink model of battery

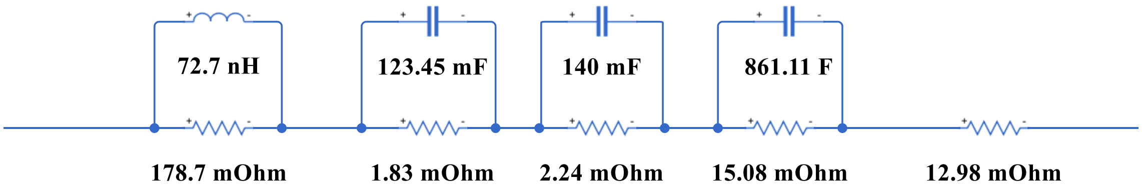

Figure 3.4: EECM of battery

3.3.2 Cable Modeling

3.3.2.1 Unshielded Cable

The unshielded cable model is taken from ELAND cables, a cable-manufacturing company for automotive applications. The cable model is FHL2G. The cable has a voltage rating of 1 kV with a nominal cross-sectional area of 50 mm^2. The cable dimensions are shown in Figure 3.5.

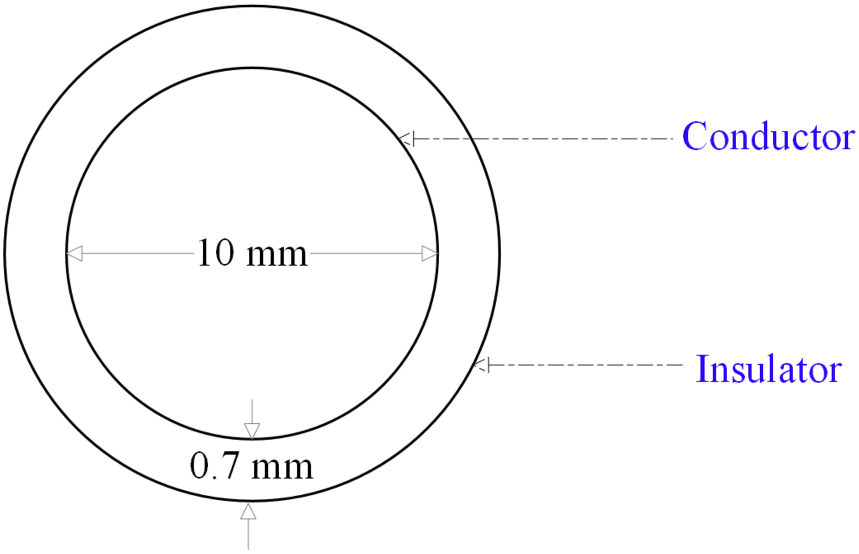

Figure 3.5: Dimension for the unshielded cable

The unshielded cables are designed using the pi-section structure. The pi-section model's key components include the series impedance and shunt admittance. The series impedance, comprising resistance (r_c) and inductance (l_c), accounts for resistive losses and inductive reactance encountered by the current. The shunt admittance, which includes capacitance (c_c), represents the capacitive coupling and leakage currents along the cable. These components together allow for an accurate simulation of a cable's distributed electrical characteristics, essential for analyzing performance under various conditions. The cables are modelled such that each pi-section represents one meter, with each block illustrated in Figure 3.6. Thus, eight sections are connected in series to represent an eight-meter cable. The two pi-sections correspond to the positive and negative DC power cables in the setup. The cable parameters were calculated using a frequency-dependent model in COMSOL, as detailed in Section 2.2.2 and Section 3.4.1.1 and the values are presented in Table A.1 in Appendix A.

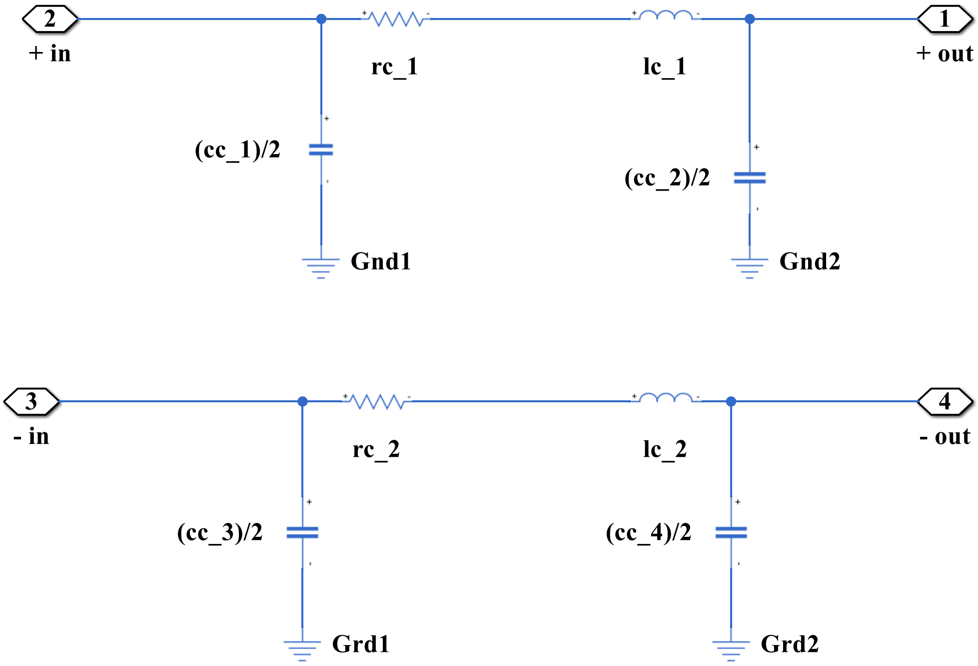

Figure 3.6: Simulink model of unshielded cable

3.3.2.2 Shielded Cable

The shielded cable model is also taken from ELAND cables and the cable model taken is FHLR2GCB2G. The cable has a voltage rating of 1 kV with a nominal cross-sectional area of 50 mm^2. The cable dimensions are shown in Figure 3.7.

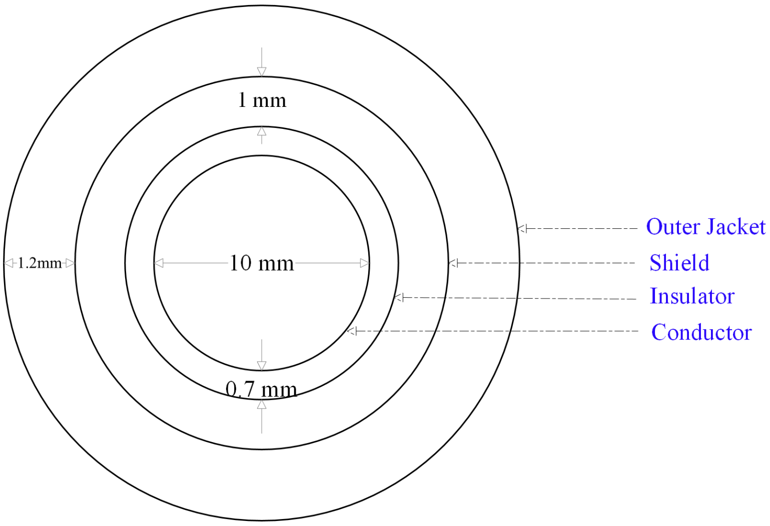

Figure 3.7: Dimension for the shielded cable

For the shielded cable, the pi-section model is modified to incorporate the effects of the shield. The shield introduces additional components: a resistance (r_s) and a self-inductance (l_s). These elements, combined with the conductor's resistance (r_c), self-inductance (l_c), and the shunt capacitance (c_c), form the comprehensive pi-section model for the shielded cable as depicted in Figure 3.8.

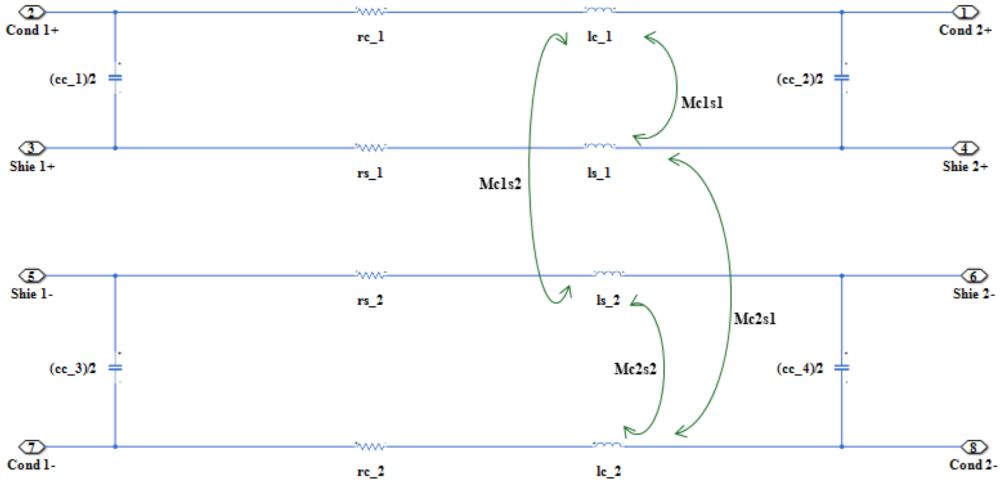

Figure 3.8: Simulink model of shielded cable

Due to the presence of the shield, mutual inductances arise between the shield and the conductor of the same cable (M_{c1s1}), as well as between the shield of one cable and the conductor of another cable (M_{c1s2}). These mutual inductances are accounted for in the model through the coupling factor, ensuring an accurate representation of the electromagnetic interactions.

Similar to the unshielded cable model, the shielded cable model is designed to represent one-meter sections. The parameters for resistance, inductance, and capacitance are calculated using frequency-dependent COMSOL simulations as described in Section 2.2.2 and Section 3.4.1.2, with detailed results provided in Table A.2 in Appendix A.

3.3.3 Inverter Modeling

The inverter is designed using the Converter block of Simulink as depicted in Figure 3.9. The "Converter (Three-Phase)" block settings in Simulink offer a detailed configuration for simulating a three-phase inverter. The block uses Insulated Gate Bipolar Transistor (IGBT)s as the switching devices, known for their efficiency and fast switching. The inverter implemented is a two-level inverter.

The PWM Generator block in Simulink is configured to provide control signals for the inverter. The generator type is set to a three-phase bridge with six pulses to ensure appropriate control of the inverter. The carrier wave is generated in an unsynchronized mode with a switching frequency of 25 kHz. The reference signal is generated internally with a natural sampling technique, directly comparing the reference signal with the carrier waveform to produce PWM pulses. A modulation index of 0.8 determines the amplitude of the reference signal, impacting the inverter's output voltage. The reference signal frequency is set to 800 Hz, matching the fundamental frequency required by the motor driven by the inverter.

A DC-link capacitor of 600 μF is used. DC-link capacitors serve as critical components in battery-fed PWM inverter systems. They act as filters, preventing high-frequency currents from flowing back into the battery and stabilizing the DC-link voltage to minimize interference with other components. Proper design of DC-link capacitors is essential to handle the current ripple and ensure the efficient operation of the inverter system [19].

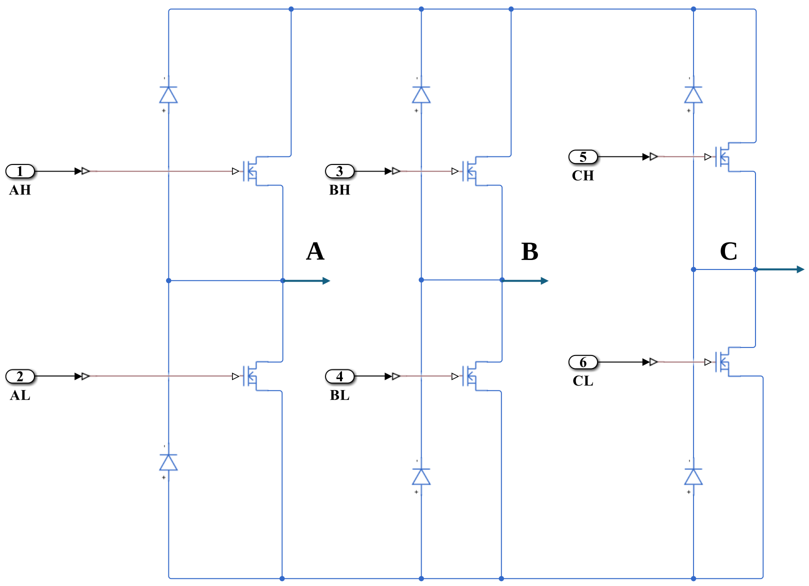

Figure 3.9: Simulink model of inverter

3.3.4 Motor Modeling

Utilizing an *RL* (resistance and inductance) load in Simulink to represent an electric motor effectively captures the motor's fundamental electrical characteristics. This technique simplifies the motor's complex dynamics into manageable elements, where resistance mimics the armature resistance and inductance reflects the motor's inductive properties, which are essential for understanding the flow of current and the development of the magnetic field. This method is particularly beneficial for simulations that do not require detailed mechanical dynamics of the motor [20].

A study from the University of Michigan [21] indicates that using *RL* components facilitates the straightforward application of Kirchhoff's and Newton's laws to simulate the electrical and mechanical aspects of the motor system in a simplified manner.

This model is adequate for many control and performance analysis applications, providing a balanced approach between simplicity and precision. This method is often sufficient for early design and testing phases, offering quick insights and aiding in the iterative design process.

The *RL* load taken in our study is shown in Figure 3.2 and is configured with specific parameters to model a wye-connected load depicting a Permanant Magnet Synchronous Machine (PMSM) machine. The rated voltage is calculated as 323 V, based on the load's characteristics. The active power is set to 260 kW and the inductive reactive power to 162.15 kVA, so that the power factor is 0.85.

In addition to the aforementioned blocks, current measurement blocks are included on the DC side of the inverter, positioned both before and after the cable model. These blocks enable visualization and quantification of the DC ripple current. The setup also incorporates a spectrum analyzer with a sampling frequency inherited from the Simulink solver with a Blackman-Harris window configuration.

3.4 COMSOL model

COMSOL Multiphysics is a versatile simulation software platform used for modelling and solving complex engineering and scientific problems. It allows users to create physics-based models with the help of predefined interfaces, covering areas such as electromagnetics, structural mechanics, acoustics, fluid dynamics, and chemical engineering. The software is known for its multiphysics capabilities, enabling the coupling of different physical phenomena to accurately simulate real-world behaviour. With its intuitive graphical user interface and powerful solvers, COMSOL is widely used in research, development, and education across various industries. It supports custom scripting and integration with other software tools, making it a comprehensive solution for advanced computational modelling tasks.

In this thesis, COMSOL software is employed for the high-frequency modelling of cables, as creating a frequency-dependent model is particularly challenging. This software is used to compare shielded and unshielded cables by simulating two DC cables carrying positive and negative currents alongside a victim cable. The induced voltage in the victim cable is then analyzed using COMSOL.

3.4.1 Cable modeling for parametrization

3.4.1.1 Unshielded cable

The unshielded cable is modelled as shown in Figure 3.10a. This model is created in 2D to minimize computation time while delivering results comparable to a 3D model. The cable consists of an inner conductor made of copper and an outer insulator jacket composed of Cross Linked Polyethylene (XLPE). A copper ground plane is situated 50 mm below the cable. The meshing is chosen to be a boundary layer meshing to capture the skin effect occurring at high frequencies with greater accuracy and is shown in Figure 3.10b.

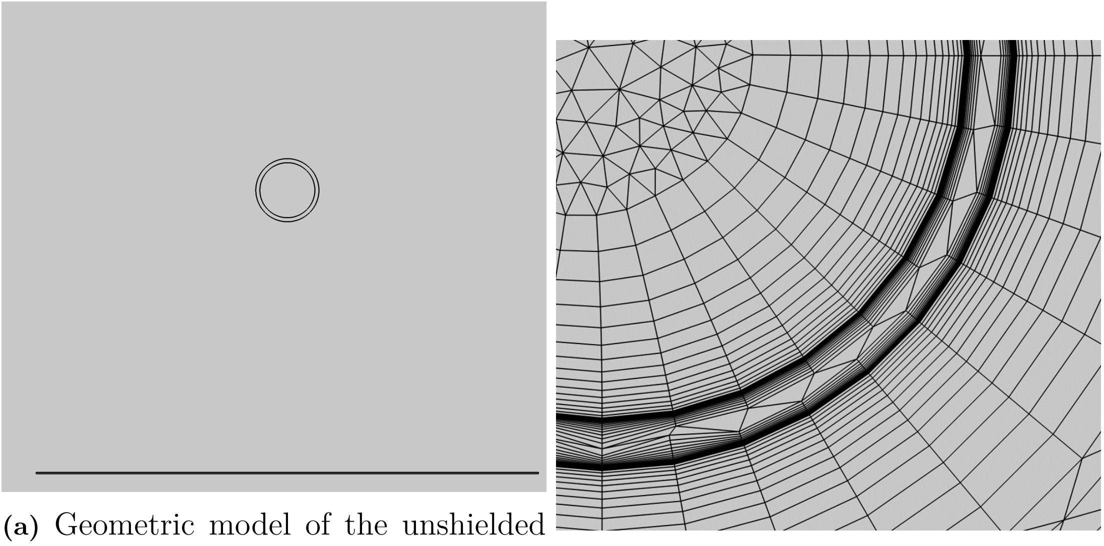

(a) Geometric model of the unshielded cable

(b) Mesh settings of the unshielded cable

Figure 3.10: COMSOL model of the unshielded cable

The materials are modeled as frequency-dependent using the Lorentz-Drude model, where the relative permittivity is a function of frequency, as discussed in Section 2.2. The setup is configured to parameterize the cable and determine the resistance, inductance, and capacitance values as functions of frequency. These values are subsequently plotted against frequency. In the Simulink cable modelling, the instantaneous values at 25 kHz are selected, and a pi-section cable model is constructed for this frequency due to its relevance at the switching frequency. This frequency is particularly significant because it tends to generate higher EMI [22].

In this study, COMSOL's magnetic fields and electric currents physics modules are utilized. Magnetic field physics is employed to determine the resistance and inductance of the cable across different frequencies. A current of 1 A is applied to the conductor part of the cable. Equation (2.8) is used to calculate the inductance based on the total magnetic energy stored, while Equation (2.9) is employed to find the resistance by integrating the copper area and the volumetric loss density. Furthermore, the electric currents physics module is used to determine the capacitance. An electric potential of 1 V is applied to the conductor, and a ground potential is assigned to the ground plane in the geometry. Equation (2.6) is used to calculate the capacitance based on the total electric energy stored.

3.4.1.2 Shielded cable

A similar setup, as discussed in Section 3.4.1.1, is modelled for the shielded cable and is shown in Figure 3.11. The primary difference is the inclusion of a metallic shield made of aluminium. The same method is employed to find the resistance, inductance, and capacitance of both the conductor and the shield. In the magnetic field physics module, a current of 1 A is applied to the conductor, while the shield is set to 0 V using voltage excitation. The conductor's self-inductance is determined by integrating the magnetic energy stored in the conductor and the insulator area around it, while the shield's self-inductance is found by integrating the magnetic energy stored in the shield area (2.8). Similar to the unshielded case, the resistance of the conductor and shield is calculated by integrating the copper area of each and deriving the values from the volumetric loss density in these areas (2.9).

Finally, the mutual inductance between the shield and conductor of the same cable, as well as the mutual inductance between the shield of one cable and the conductor of a nearby cable, is found by integrating the magnetic energy in the shield and conductor areas with a similar configuration in magnetic field physics. The capacitance is calculated using (2.6) based on the total electrical energy stored.

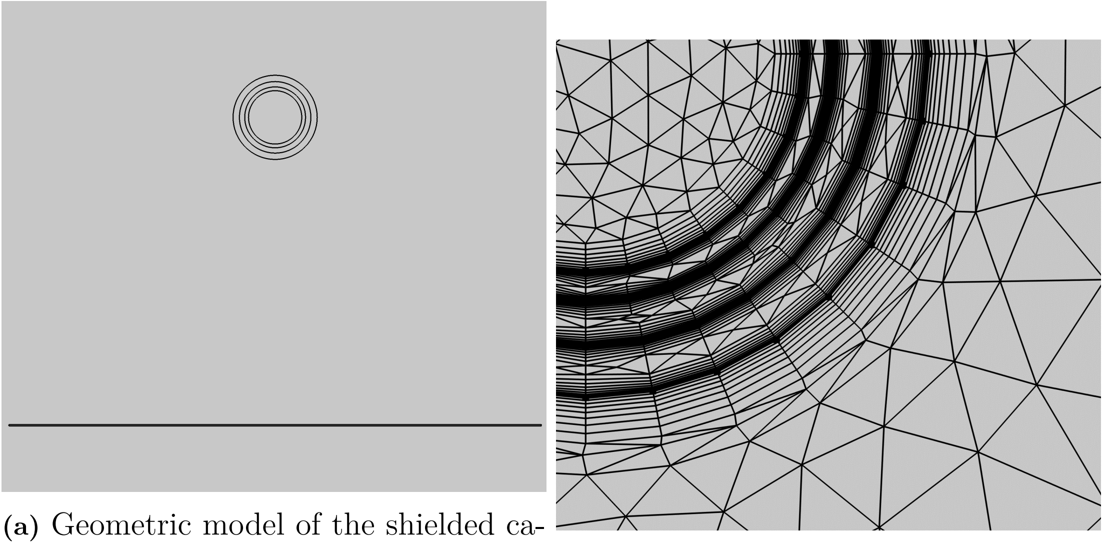

(a) Geometric model of the shielded cable

(b) Mesh settings of the shielded cable

Figure 3.11: COMSOL model of the shielded cable

3.4.2 Modeling of the Cable for Parametric Distance Sweep

The setup for conducting the parametric distance sweep for both shielded and unshielded cables is depicted in Figure 3.12. Initially, the two power cables carrying positive and negative currents are positioned 150 mm apart. The victim cable, which is the focus of the induced voltage analysis, is placed 100 mm vertically above the power cables, centred between them. This positioning ensures that the victim cable is equidistant from both power cables. To analyze the effect of varying distances between the power cables on the induced voltage in the victim cable, the parametric sweep is performed in COMSOL. The distance, as shown by the dotted line, is gradually decreased from 150 mm to 130 mm, then to 100 mm, followed by 80 mm, and finally to 60 mm in the direction indicated by the red arrows and also by keeping the victim cable at a constant position. At each distance, the induced voltage in the victim cable is measured.

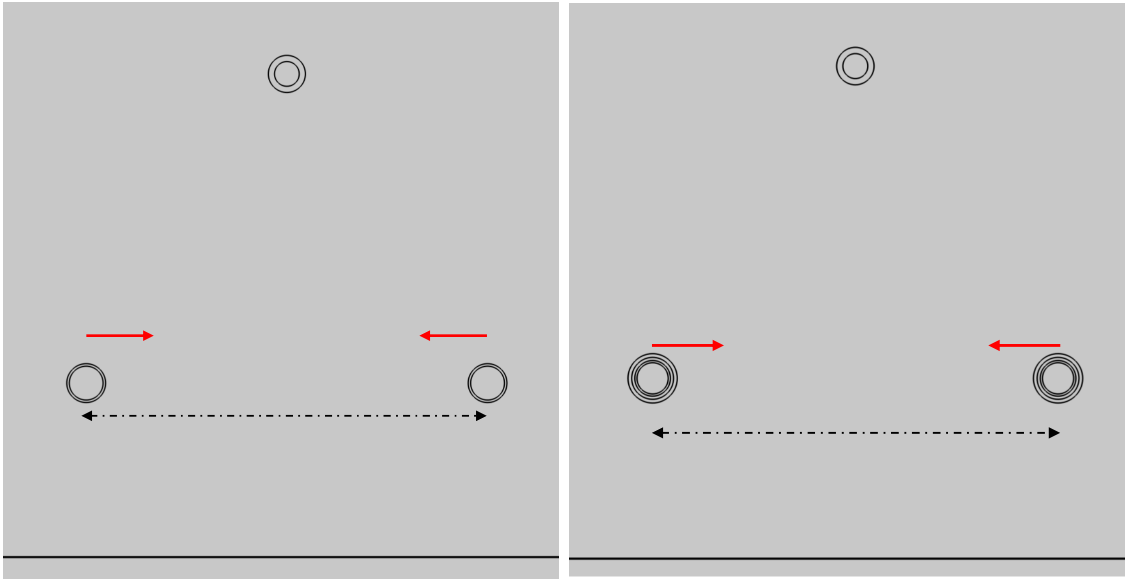

(a) Unshielded DC power cables with a victim cable **(b)** Shielded DC power cables with a victim cable

Figure 3.12: Power cables modeled with a victim cable

For this setup, the magnetic fields physics module in COMSOL is utilized, where the conductors are supplied with positive and negative currents, and the shield is maintained at ground potential. The applied currents are DC with ripple, simulated using Simulink based on the model illustrated in Figure 3.2. This current profile is critical for creating a realistic and accurate representation of the system's operational conditions.

In the Simulink model, both unshielded and shielded cables are simulated to capture the detailed current profiles under these configurations. These current profiles are then used as inputs for the COMSOL simulation. This approach allows for a comprehensive examination of the electromagnetic interactions and provides a real-time analog of the actual system setup. By simulating the unshielded and shielded cables in Simulink and using the resultant currents in COMSOL, we aim to analyze the EMI characteristics more effectively. This integrated modelling approach ensures that the simulated conditions closely mimic real-world operations, thereby enhancing the accuracy and reliability of the simulation results.

4

Analysis

4.1 Frequency dependent parameters

The frequency-dependent parameters for creating a Simulink model, as shown in Section 3.3.2, are determined by modelling the cable in COMSOL, as described in Section 3.4.1.

4.1.1 Resistance

The resistance is calculated for the conductor area highlighted in Figure 4.1a. Equation (2.9) is used for calculation of resistance which integrates the copper area and the volumetric loss density and this is done by feeding a current of 1 A in COMSOL [23]. The graph displayed in Figure 4.1b shows the variation of the resistance per meter of an unshielded DC power cable as a function of frequency.

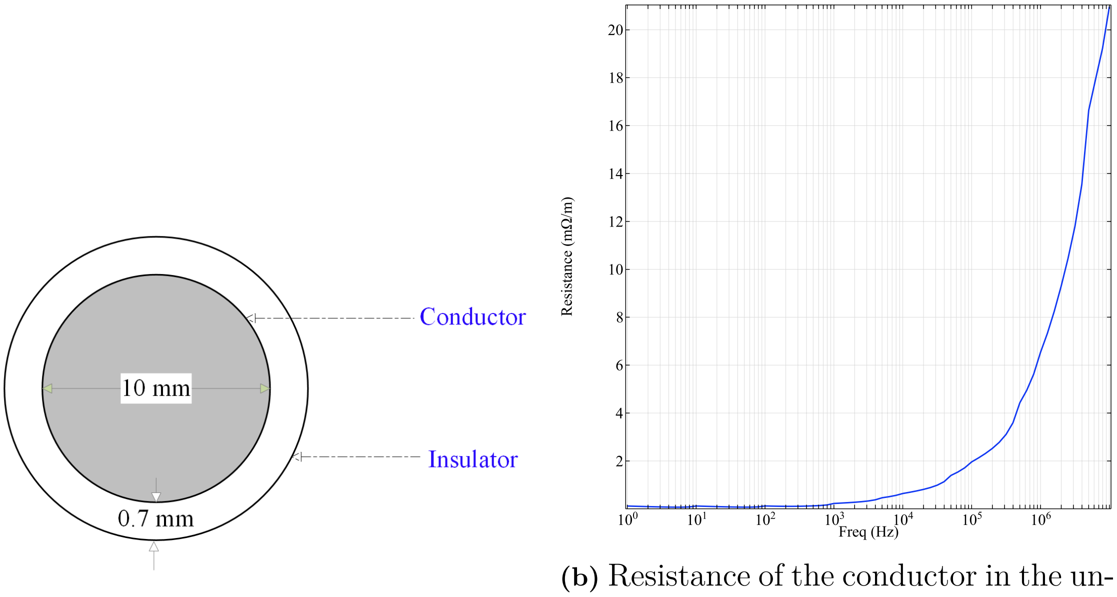

(a) Conductor area to be integrated

(b) Resistance of the conductor in the unshielded cable

Figure 4.1: Frequency dependent resistance for the unshielded cable

The resistance values span from 1 Hz to 10 MHz, indicating a significant increase in resistance with rising frequency. This behaviour is predominantly attributed to the skin effect explained in Section 2.2.3 and other frequency-dependent phenomena affecting the conductive materials of the cable. At low frequencies, the resistance of the conductor remains relatively constant. This is because the current distribution across the cross-sectional area of the conductor is uniform, allowing the entire cross-section to contribute to the conduction of electric current. However, as the frequency increases, the skin effect becomes more pronounced [24]. As frequency increases, the conductivity of the conductor effectively decreases due to the skin effect. Current tends to flow near the conductor's surface, reducing the effective cross-sectional area available for current flow. This phenomenon leads to an increase in the conductor's resistance with frequency.

The graph also reflects the inherent material properties of the conductor and insulating materials used in the cable. As frequency increases, the dielectric properties of the insulation play a significant role, leading to additional losses. These losses, often represented by the material's complex permittivity, are a result of the imaginary part of the permittivity, related to dielectric losses, increasing with frequency, causing further energy dissipation in the form of heat within the dielectric material.

For the shielded cable, the resistance as a function of frequency is illustrated in two separate graphs: one for the conductor and one for the shield. Similar to the unshielded cable, the resistance of the conductor in the shielded cable increases with frequency, but with a less steep initial rise, as shown in Figure 4.2b. The skin effect again plays a significant role here, causing the resistance to increase sharply beyond 10 kHz and rise even more steeply beyond 100 kHz. The graph shows that the resistance of the conductor in the shielded cable reaches approximately 3.8 mΩ/m at 10 MHz.

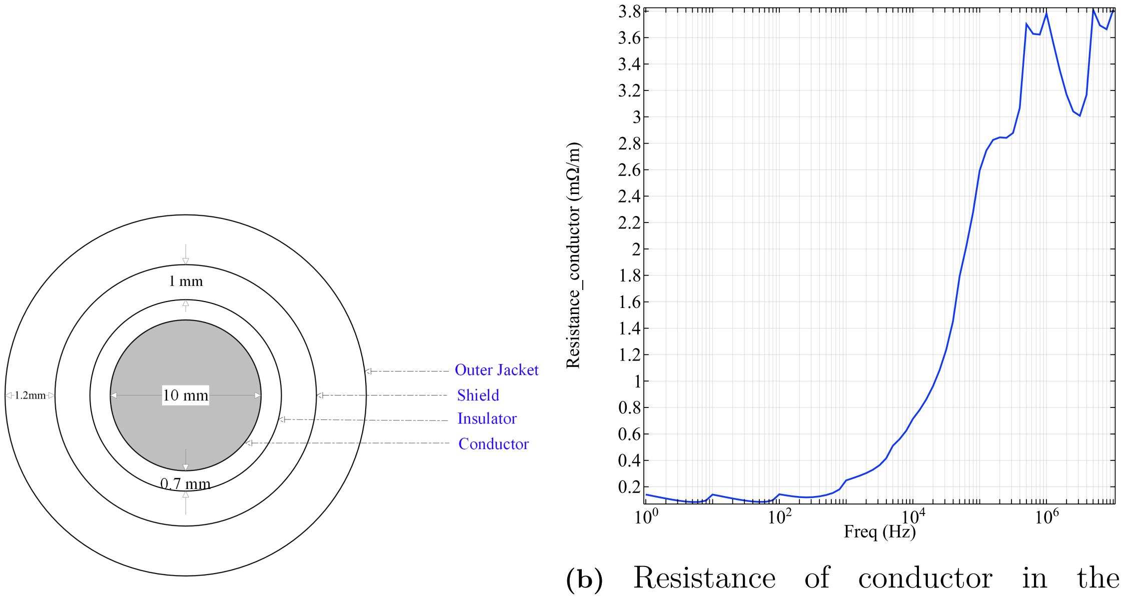

(a) Conductor area to be integrated

(b) Resistance of conductor in the shielded cable

Figure 4.2: Frequency dependent resistance of conductor for the shielded cable

The resistance of the shield, depicted in Figure 4.3b, also increases with frequency, following a similar trend but at a higher magnitude compared to the conductor. This increase is due to the same electromagnetic effects affecting the shield material, typically a less conductive material like aluminium or copper braid. The shield resistance rises steeply beyond 10 kHz, reaching approximately 7.3 mΩ/m at 10 MHz. The higher resistance values in the shield compared to the conductor can be attributed to the additional path lengths and contact resistances within the shield structure [25]. The peaks in the figures may represent the oscillatory behaviours in the electron levels because of the LD modelling of the materials used.

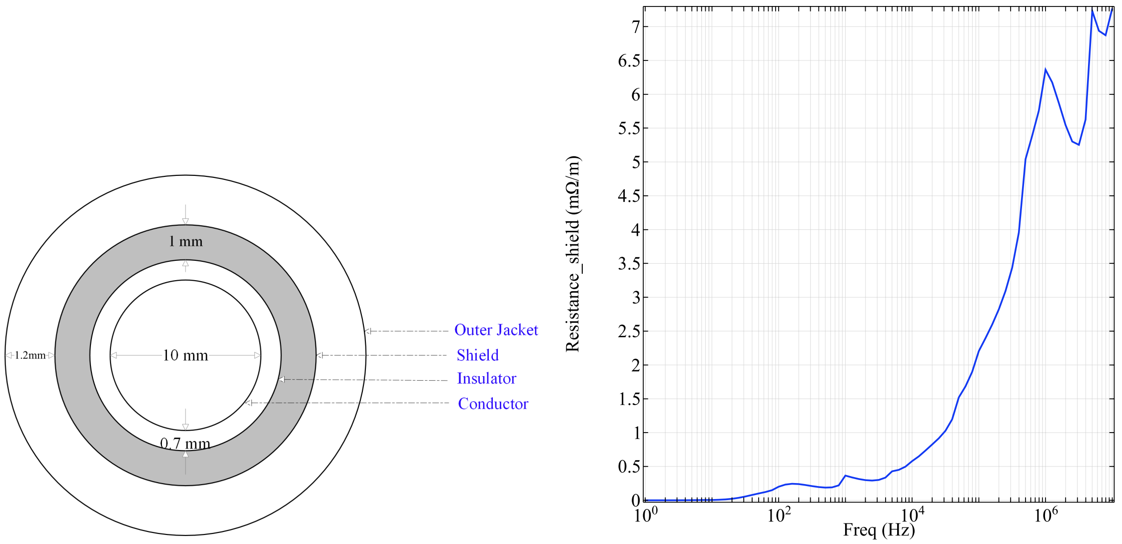

(a) Shield area to be integrated **(b)** Resistance of the shield

Figure 4.3: Frequency dependent resistance of shield for the shielded cable

4.1.2 Inductance

The analysis of the unshielded cable's inductance, as depicted in Figure 4.4, demonstrates a clear frequency-dependent behaviour. At lower frequencies, the inductance remains relatively constant around 765 nH/m. However, as the frequency increases, a noticeable decline in inductance is observed. This behaviour can be attributed to the skin effect.

In the analysis of shielded cables, the inductance of both the conductor and the shield is examined separately as a function of frequency. The inductance of the conductor, as depicted in Figure 4.5a, shows a significant decrease with increasing frequency. At lower frequencies, the inductance remains relatively constant at approximately 75 nH. However, as the frequency approaches the MHz range, the inductance sharply drops, indicating a significant reduction in the inductive reactance due to the skin effect, which limits the current flow to the conductor's surface.

Similarly, the inductance of the shield, as shown in Figure 4.5b, exhibits a notable frequency dependency. This behaviour of inductance indicates the decreased shielding effectiveness at higher frequencies, where the inductive reactance of the shield

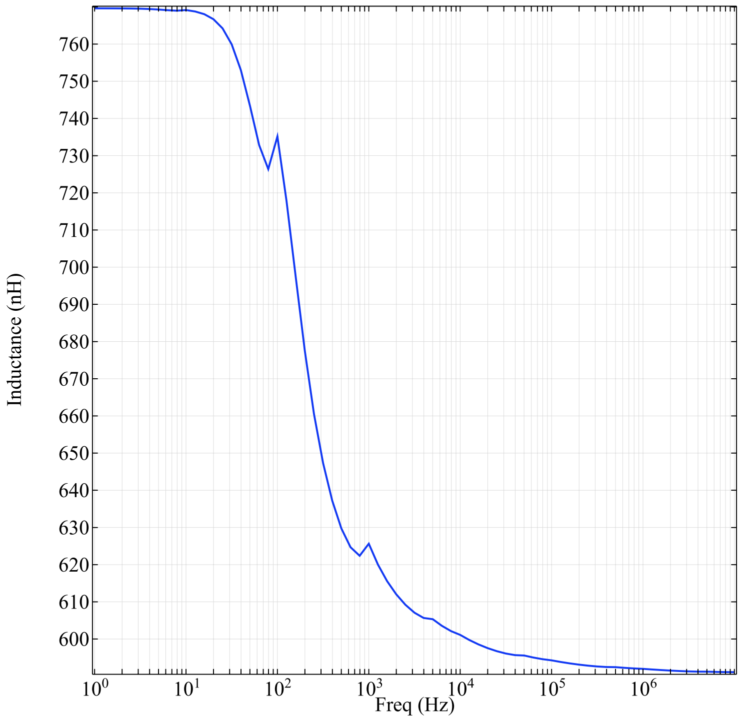

Figure 4.4: Frequency dependent Inductance for the unshielded cable

minimizes the magnetic coupling between the conductor and the external environment.

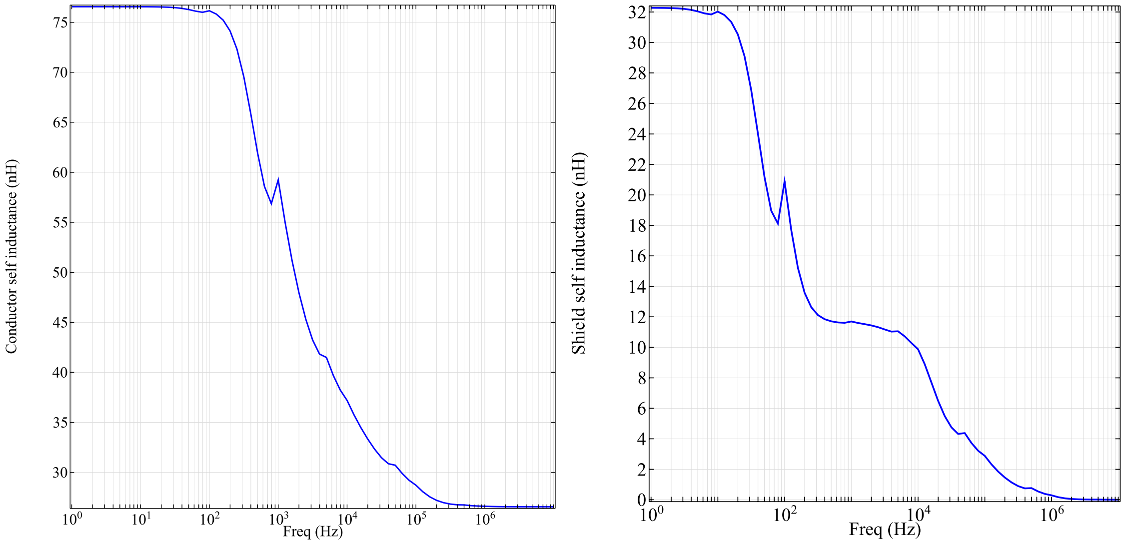

(a) Self Inductance of the conductor **(b)** Self Inductance of the shield

Figure 4.5: Frequency dependent inductance for the shielded cable

There is a significant mutual inductance between the conductor and the shield of the same cable as depicted in Figure 4.6a, and also, there exists a mutual inductance between the conductor of the positive current carrying cable and the shield of the negative current carrying cable in the setup in Figure 4.7a, which must be taken into account during modelling to ensure accuracy. This mutual inductance illustrated in Figure 4.6b and Figure 4.7b demonstrates its frequency dependent behaviour and impact on the overall system performance.

These observations underscore the importance of considering the frequency-dependent behaviour of inductance in the design and analysis of shielded cables, particularly for high-frequency applications where EMI is a concern. The reduction in inductance with frequency enhances the shielding capability, thereby providing better protection against high-frequency noise and ensuring the integrity of the signal transmission. A detailed understanding of these parameters is crucial for optimizing cable performance in electrical systems subjected to varying frequency conditions.

In the COMSOL model for the cable, the shunt capacitance remains constant and does not vary with frequency. This consistency is maintained across all frequencies, ensuring that the capacitive effects in the cable are accurately represented. The unchanging nature of the shunt capacitance simplifies the analysis and provides a stable parameter for modelling the cable's behaviour in different frequency scenarios. The measurements indicate that the capacitance for the unshielded cable is 16 pF/m, while the shielded cable shows a capacitance of 1236 pF/m.

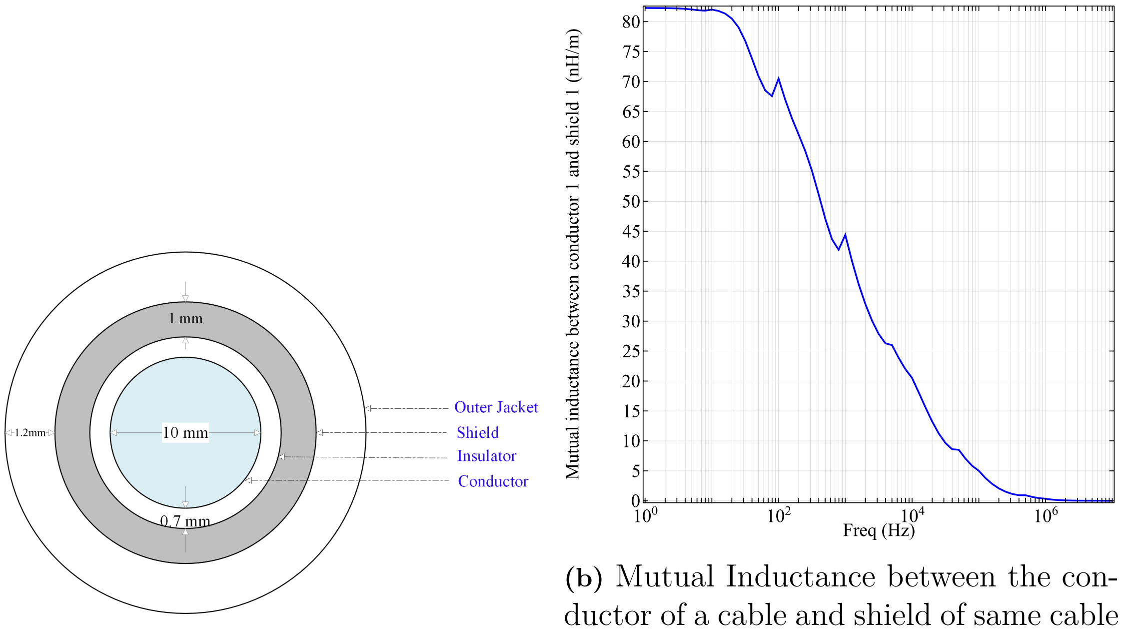

(a) Area integrated for inductance

(b) Mutual Inductance between the conductor of a cable and shield of same cable in proximity

Figure 4.6: Frequency dependent mutual inductance between conductor and shield within the same shielded cable

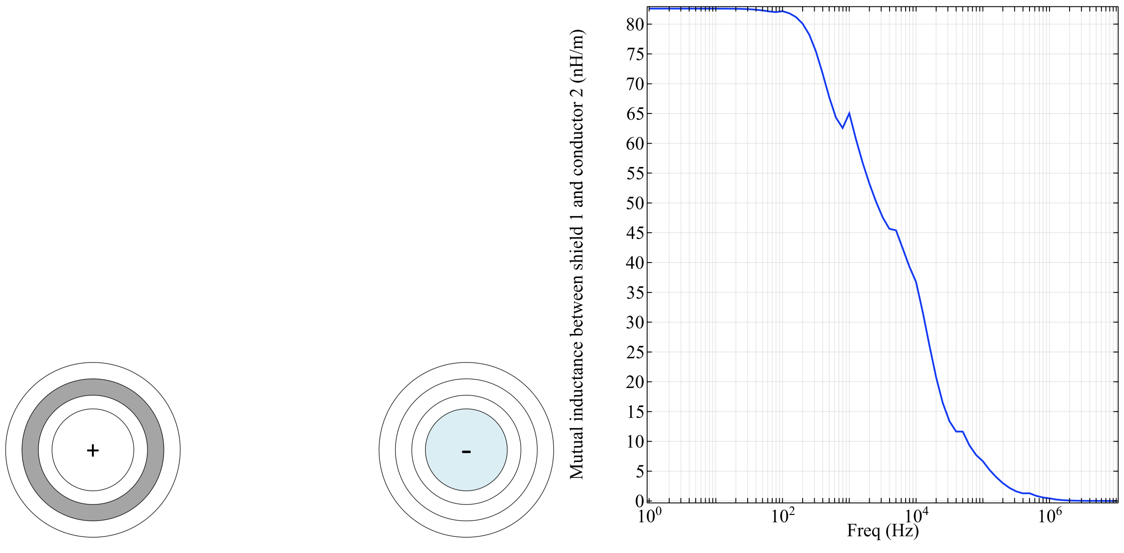

(a) Area integrated for mutual inductance

(b) Mutual Inductance between the conductor of a cable and shield of another cable in proximity

Figure 4.7: Frequency dependent mutual inductance between conductor and shield in the nearby shielded cable

4.2 Analysis of DC Ripple current and DC Voltage ripple

The model setup is based on the frequency-dependent parameters defined by the cables. The parameters of the cables were taken for 25kHz, as this was the switching frequency of the inverter. The DC current is measured at two points one before the cable and the other after the cable. The results from both the scopes were the same. So the current analysis was at the model's battery side.

The current waveform is presented in Figure 4.8a and 4.8b for the unshielded cable and shielded cable respectively. In the unshielded case, there is a peak-peak current of 130 A and an average current of 392 A according to the analysis. Additionally, the shielded cable exhibits an average current of 392 A with a peak-peak current of approximately 200 A. Considering a power electronic efficiency of approximately 95%, the input power is calculated to be 275 kW, resulting in a DC current of 387 A theoretically, under the assumption of a nominal voltage of 710V.

However, in the shielded case, it is seen that the peak-peak current is higher, around 230 A. In examining whether the DC current ripple is higher in the shielded cables compared to the unshielded ones, it is crucial to understand the impact of shielding on electrical systems. The research [26] delves into the behaviour of shielded High Voltage (HV) cables in automotive systems, noting that Differential Mode (DM) ripple currents from traction inverters can induce currents in the shielding of HV cables. This phenomenon affects the total current ripple in the system, demonstrating the complex interplay between shielded conductors and induced currents over time.

There are several reasons why the current ripple might be higher in shielded cables. One key factor is the increased capacitance resulting from the shielding layer, which can change the impedance characteristics of the cable and potentially amplify ripple currents at certain frequencies. Shielded cables typically exhibit higher capacitance due to the shield, acting as a conductive layer near the core conductor which alters the cable's electrical properties [26].

Additionally, the shielding layer can slightly increase resistance and inductance, affecting the cable's interaction with high-frequency ripple components and potentially increasing ripple under specific conditions. The shielding also influences the distribution of electromagnetic fields around the cable, sometimes causing resonance effects that can enhance ripple currents.

Ripple currents can induce various adverse effect including increased power loss, EMI and degradation of power supply components such as batteries and capacitors. These currents contribute to supplementary heating within the components, consequently reducing their overall lifetime. The magnitude and frequency components of the ripple current are dependent on the inverter's switching frequency.

The occurrence of DC ripple currents in inverter systems can be largely attributed to the high-frequency switching operations inherent in PWM techniques. Inverters convert DC to AC by rapidly switching transistors to produce rectangular voltage pulses, which in turn create current pulses in the DC bus, leading to ripple currents. The characteristics of these ripple currents are shaped by the specific PWM method used, such as Sinusoidal Pulse Width Modulation (SPWM), Space Vector Pulse Width Modulation (SVPWM), and Discontinous Pulse Width Modulation (DPWM), each introducing unique ripple patterns due to different switching sequences. The modulation index and load power factor also significantly influence the ripple current's magnitude and harmonic content, with higher modulation indices typically resulting in greater ripple magnitudes and harmonics appearing at multiples of the carrier frequency and its sidebands. The equivalent centred harmonic approach explains that the harmonic currents from inverter switching cause periodic oscillations in the DC bus, contributing to ripple currents [27].

Next, the conducted emissions from the inverter on the DC side are analyzed. The current data is obtained from the scope and processed in MATLAB for FFT analysis of the signal. The frequency spectrum is then examined from 1 Hz to 10 MHz. The calculation of conducted emissions is explained in (2.10).

The graph in Figure 4.9 clearly illustrates that the maximum emissions are observed at 25kHz, which aligns with the switching frequency of the inverter, registering a value of approximately 160 dBμA. This observation is significant as it highlights a critical point in the emission spectrum. It is also seen from Figure 4.10 that the

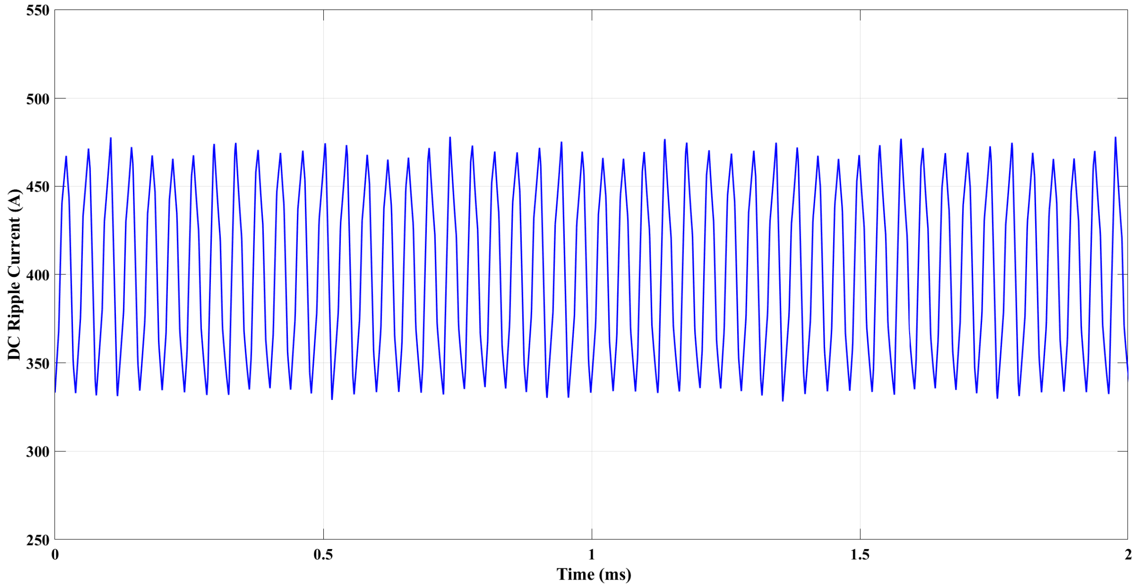

(a) DC Ripple current for the unshielded cable

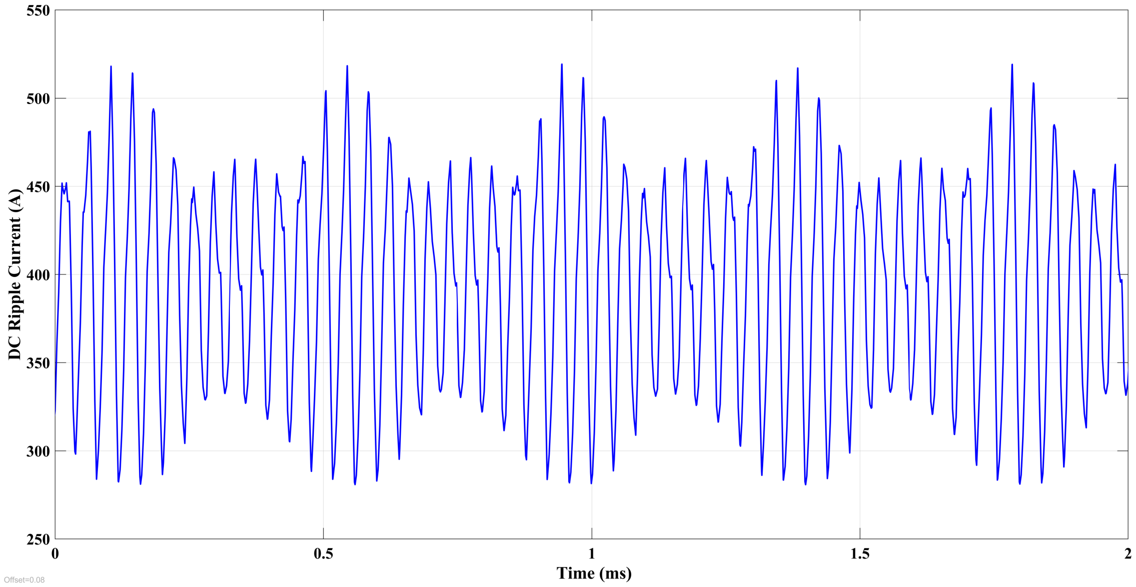

(b) DC Ripple current for the shielded cable

Figure 4.8: DC Ripple current in the battery side

CE from the shielded and unshielded cable is almost similar with few differences in the high-frequency region because the cable is the victim of the EMI from the setup illustrated. In reality, the unshielded cable are more susceptible to RE because of the electromagnetic interactions between the nearby electrical systems.

To contextualize these findings, we reference the DO-160 standards for power lines, depicted in Figure 2.3. Although these standards are specifically tailored for 270V systems, they nonetheless provide a valuable benchmark for understanding emission levels in electric aircraft systems. By comparing the emission levels presented, it becomes evident that the emissions for the 260 kW system are notably high. This comparison underscores the considerable nature of the emissions at this particular power level, suggesting a potential area of concern for compliance and performance in electric aviation applications.

The voltage ripple is also analyzed at a point 3m away of the battery for both unshielded and shielded cable and shown in Figure 4.11 . This specific distance is chosen as this is the place where the PDU is placed. The voltage ripple at the PDU is analysed as this ripple could be experienced by other 800V systems connected to it. Similar to the current ripple, the voltage ripple in the shielded cable is slightly higher for similar reasons. The FFT of the voltage ripple showing the high-frequency components are shown in Figure 4.12. This indicates that if the voltage ripple experienced by the loads connected to the same bus as the battery is elevated, the components connected to that bus will be adversely impacted.

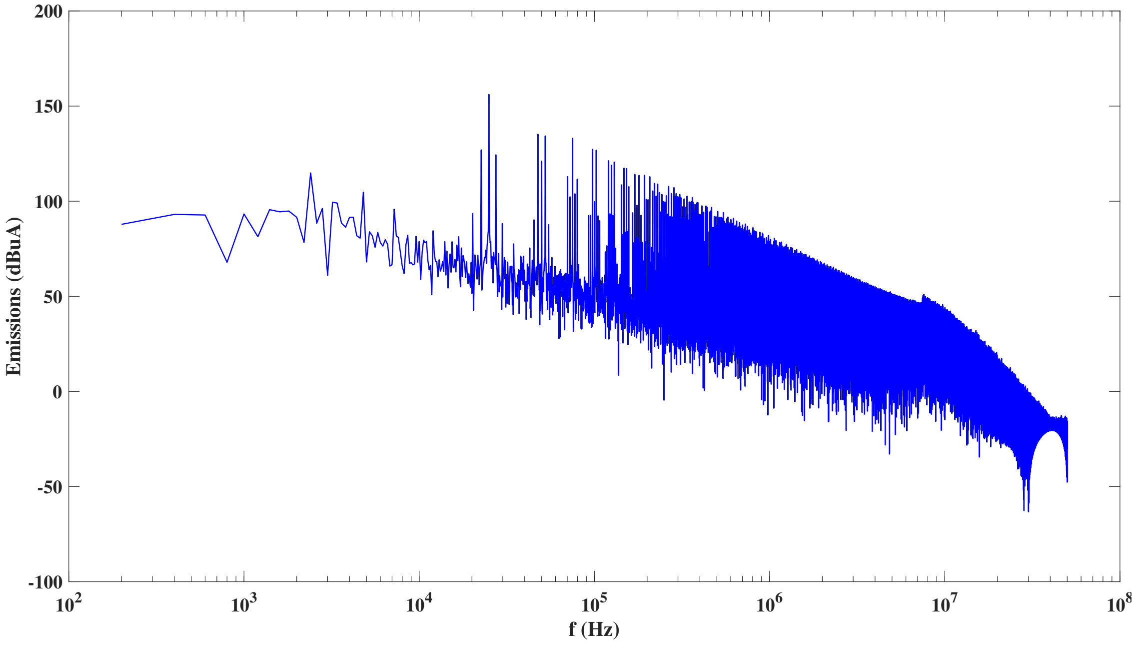

Figure 4.9: Conducted Emissions for the unshielded cable

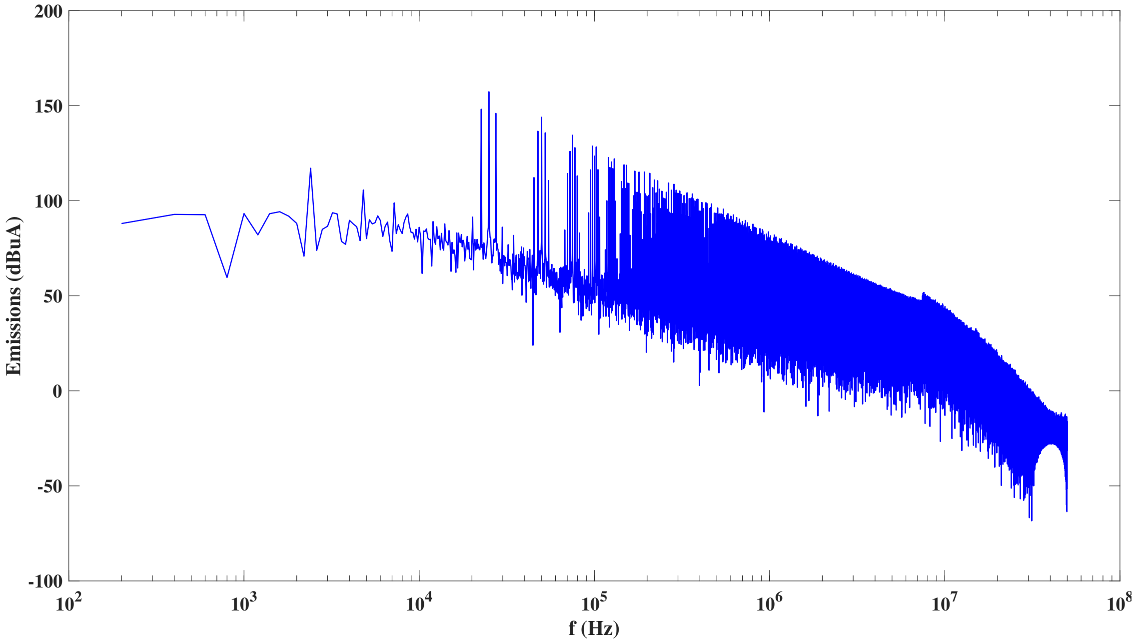

Figure 4.10: Conducted Emissions for the shielded cable

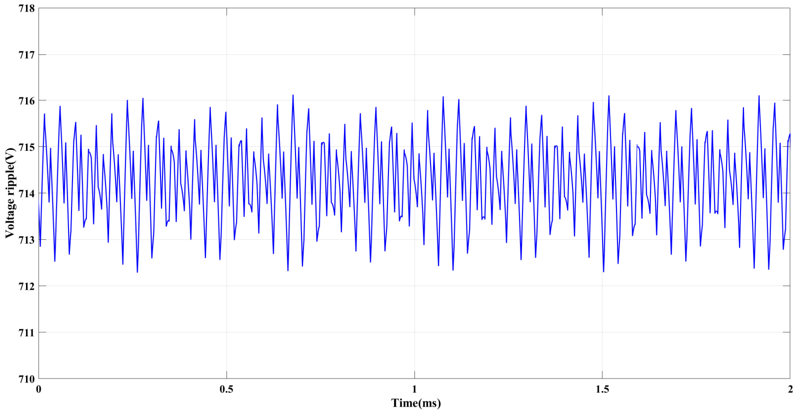

(a) Voltage Ripple for the unshielded cable at PDU

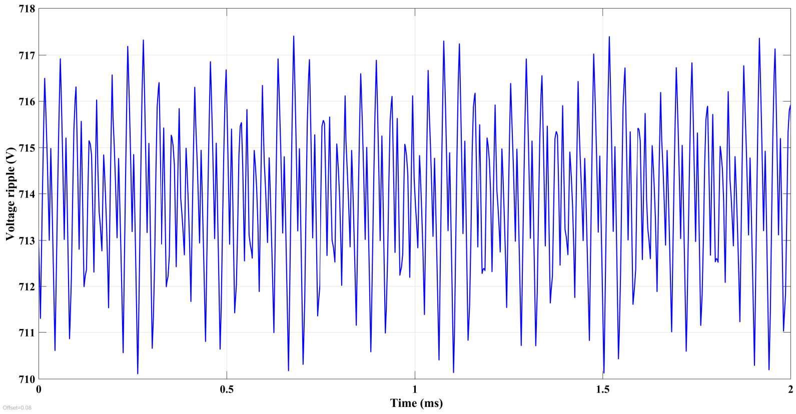

(b) Voltage Ripple for shielded the cable at PDU

Figure 4.11: Voltage Ripple at PDU located 3m away from the battery

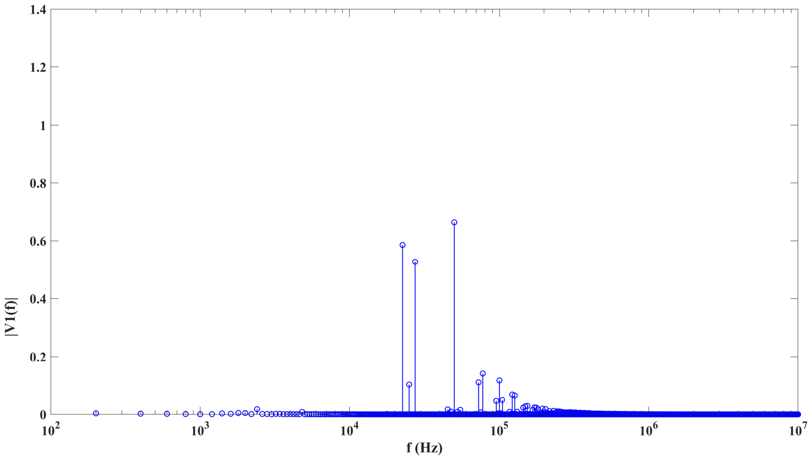

(a) FFT of Voltage Ripple for unshielded cable at PDU

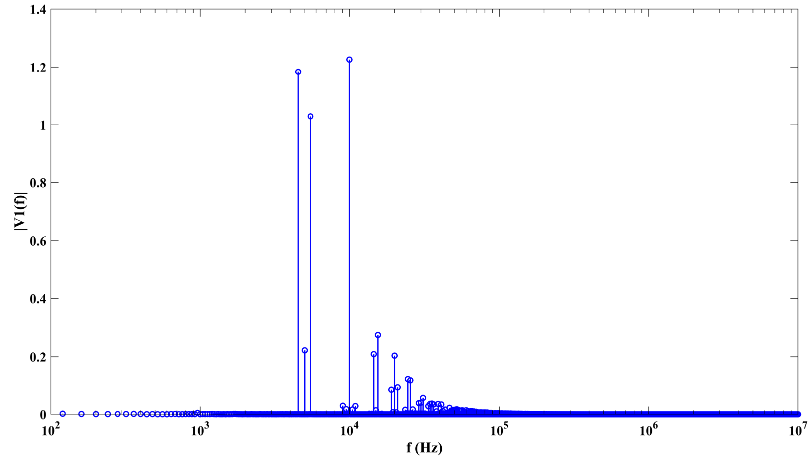

(b) FFT of Voltage Ripple for shielded cable at PDU

Figure 4.12: FFT of Voltage Ripple at PDU located 3m away from the battery

4.3 Analysis of ESR in DC Link Capacitor

The load characteristics and the performance of the DC bus capacitor play crucial roles in determining the extent of ripple currents. The DC bus capacitor's role is to smooth out these ripples, but its effectiveness depends on its capacitance value and ESR. Insufficient capacitance or high ESR can result in inadequate smoothing, allowing significant ripple currents to remain [28]. Furthermore, the inverter's switching frequency and the interactions between the switching devices and passive components, like inductors and capacitors, create complex impedance paths that affect the ripple currents.

The effect of ESR of the DC Link capacitor on CE is studied in this section. Selecting a good capacitor while designing inverter systems is essential in controlling the emissions. The studies are done for the values of 1 $\mu\Omega$, 1 mΩ and 1 Ω. The CE for the different values of ESR is shown in Figure 4.13 and the images shown are in the higher frequencies ranging from 1 MHz to 1.25 MHz. From the figures it can be seen that as the ESR is reduced the emissions are reduced at higher frequencies. In high-frequency electronic circuits, ESR of capacitors plays an important role in controlling EMI. It is important to note that the values of 1 Ω and 1 $\mu\Omega$ are unrealistic but these values are chosen to show the importance of selecting a suitable DC Link capacitor for a converter system. Capacitors with low ESR are crucial for effectively filtering out high-frequency noise, as they offer a minimal resistance path for these unwanted signals.

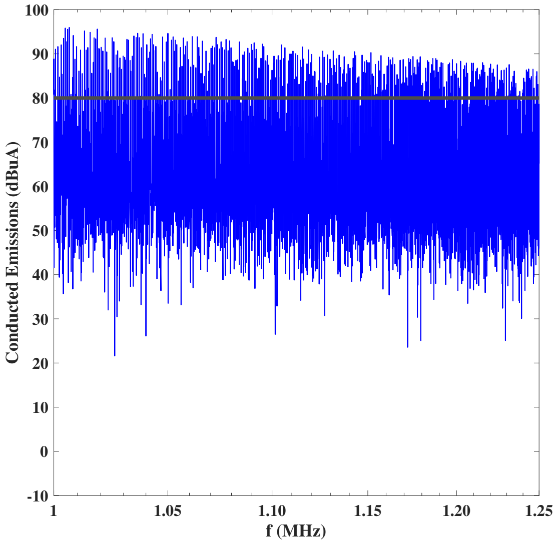

(a) ESR of 1 Ω

(b) ESR of 1 $\mu\Omega$

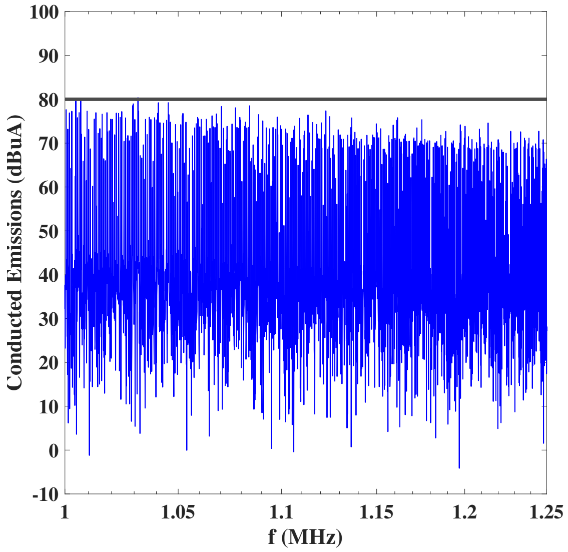

(c) ESR of 1 mΩ

Figure 4.13: Conducted Emissions measurement with different ESR in DC Link capacitors

4.4 Analysis of induced voltage in the victim cable

COMSOL analysis of the effect in the victim cable because of the power lines is explained. The setup is done as described in Section 3.4.2. The initial analysis compares the induced voltages in unshielded and shielded cables. The voltages are assessed at five different distances, ranging from 150mm to 60mm. This is achieved by adjusting the proximity of the two power cables, as illustrated in Figure 3.12.

Induced voltage in the victim cable because of the DC power cables is shown in Figure 4.14 and Figure 4.15 for the unshielded and the shielded case respectively. The trend for both unshielded and shielded shows that the induced voltage is reduced as the cables are brought closer to each other. This study shows that the DC power cables can be kept as close as possible to each other so that the voltage induced in the neighbouring cables, i.e. the victim cable placed vertically above, is less affected. This effect is critical in designing systems where precise control of induced voltages is necessary, such as in power transmission and distribution networks. Furthermore, understanding this interaction is essential in EMC studies to minimize unwanted induced voltages that could interfere with sensitive electronic equipment.

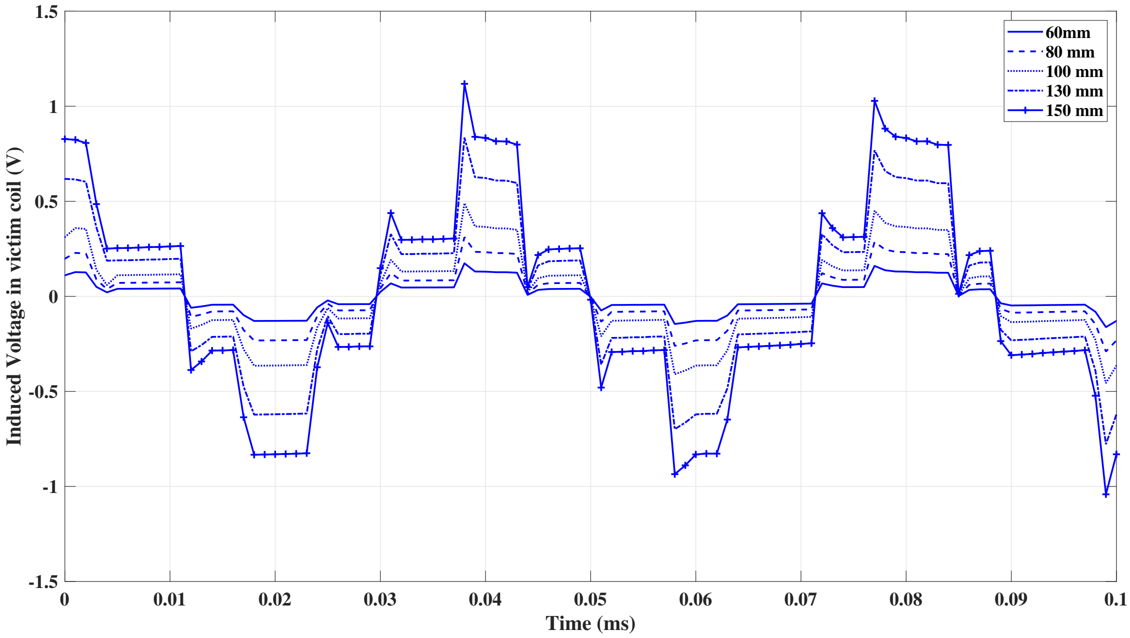

Figure 4.14: Induced voltage in victim cable with the unshielded cable

The comparison of shielded and unshielded is studied further. This study was conducted to compare the effect of shielded cables to unshielded ones. The comparison is taken for a selected distance of 130 mm and shown in Figure 4.16. The FFT of the induced voltage is shown in Figure 4.17. It is evident from Figure 4.17 that the component at the switching frequency of the inverter (25 kHz here) is high and

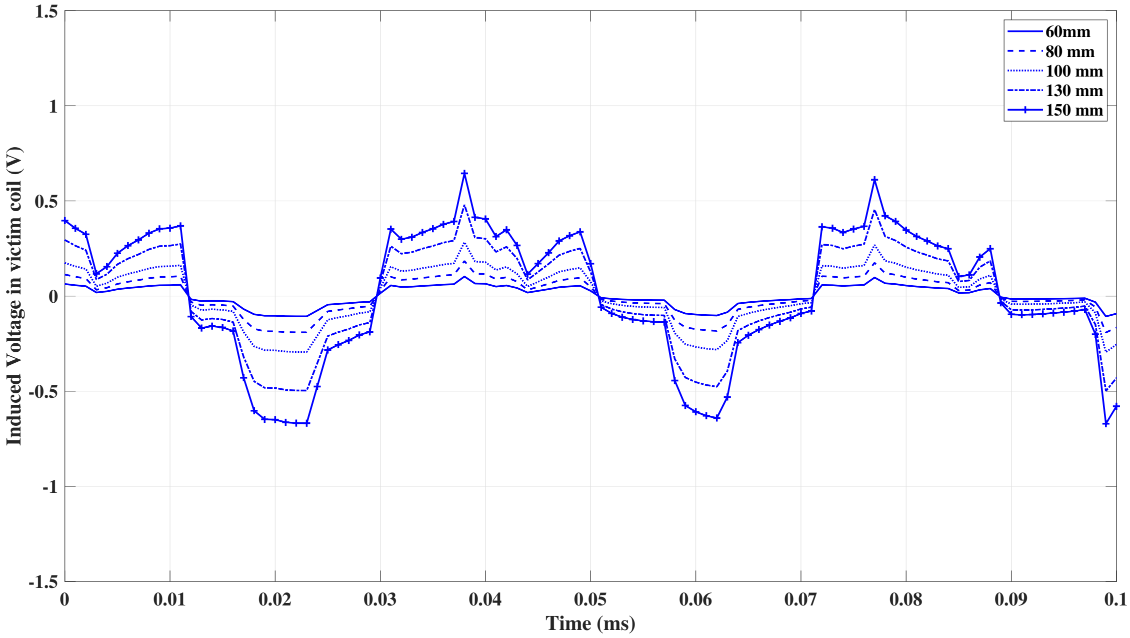

Figure 4.15: Induced voltage in victim cable with the shielded cable

the unshielded cable has a lesser voltage magnitude. Shielded cables offer substantial benefits in mitigating EMI compared to unshielded cables. A key advantage is the reduction of radiated EMI, which is critical for maintaining signal integrity in environments with significant electromagnetic noise. Another significant advantage of shielded cables is the enhancement of overall system performance and reliability through the reduction of crosstalk between adjacent cables. Crosstalk, which can cause signal degradation and data loss, is minimized due to the protective barrier provided by the shielding material. This is particularly important in environments where multiple cables are routed closely together, such as in data centres or industrial control systems.

Moreover, the shielding layer, which can be made of materials such as copper, aluminium, or conductive polymers, provides an effective grounding path that further reduces the potential for electromagnetic interference. The effectiveness of the shielding is influenced by factors such as the conductivity and permeability of the shielding material and the frequency of the interfering signal. Multilayered composite shields, for instance, utilize different materials to maximize shielding effectiveness across a wide frequency range.

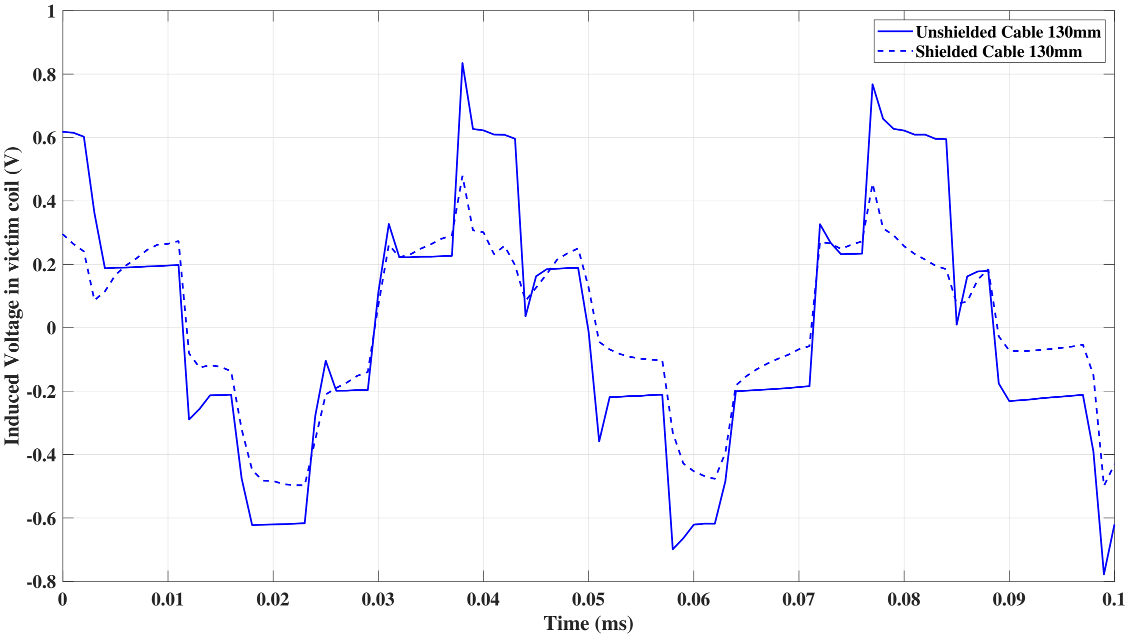

Figure 4.16: Induced voltage - Shielded vs Unshielded

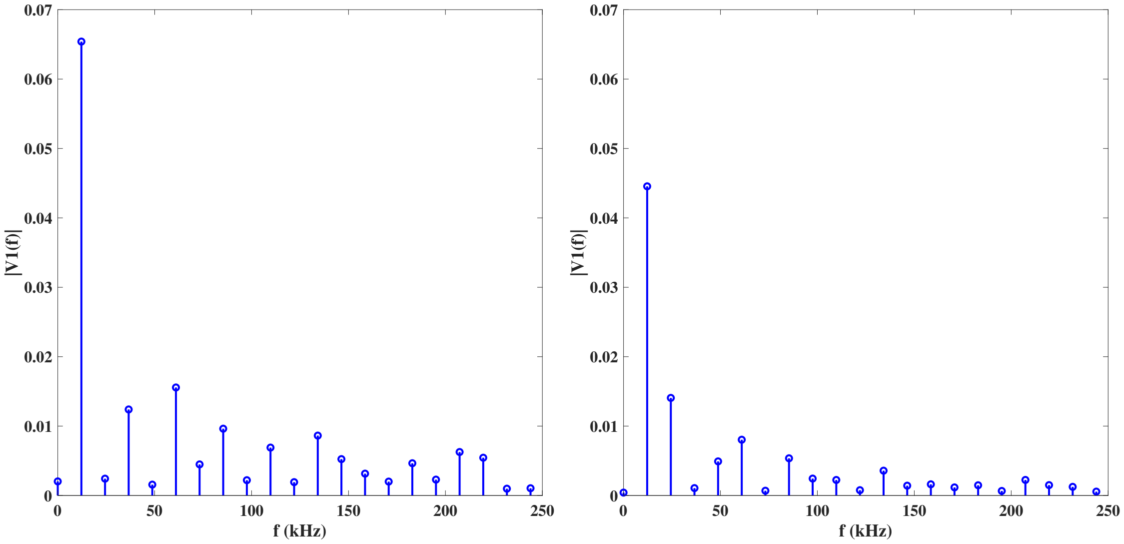

(a) FFT of induced voltage with the unshielded cable

(b) FFT of induced voltage with the shielded cable

Figure 4.17: FFT of induced voltage in the victim cable

5

Conclusions

5.1 Results

This thesis has provided a comprehensive analysis of the EMI characteristics of DC power cables in electric aircraft systems, focusing on both shielded and unshielded cables. Through detailed simulations and measurements, the study explored the behaviour of these cables from 1 Hz to 10 MHz, highlighting the significant impact of high-frequency phenomena on EMI performance.

Key findings revealed that unshielded cables exhibit considerable EMI at the inverter's switching frequency of 25 kHz, with emissions reaching approximately 160 dBμA. The peak-peak ripple was quantified and for the unshielded cable a ripple current of 140 A was measured. While shielded cables demonstrated improved EMI mitigation, challenges persisted at higher frequencies due to increased capacitance, resistance, and inductance. The study also showed that closer cable arrangements reduced induced voltage in the victim cable through magnetic field cancellation with a reduction in the induced voltage of around 85%, thus enhancing EMI performance. However, the analysis indicated that shielded cables experienced higher DC ripple currents of around 230 A due to the complex interactions of induced currents within the shielding layer. The effect of ESR of the DC-Link capacitor is analyzed and it was found that the CE reduced in the higher frequency ranges as ESR reduced.

Furthermore, the research emphasized the necessity of effective shielding and adherence to standards like DO-160 to manage conducted emissions in electric aircraft systems. The detailed simulations provided valuable insights into the high-frequency effects that must be considered in the design of DC power cable systems to ensure optimal performance and compliance with regulatory standards in electric aviation.

Overall, this thesis underscores the importance of considering electromagnetic emissions in the design and implementation of electric propulsion systems.

5.2 Future work

Given the comprehensive analysis and significant findings of this study, several areas for future work are identified to further enhance understanding and mitigation of EMI in electric aircraft systems. While this thesis primarily relied on simulations, practical testing is crucial for validating the simulation results. Conducting experiments in real-world conditions will help identify any discrepancies between the theoretical models and actual performance, ensuring the robustness and reliability of the findings. Additionally, future research should include practical setups to measure RE, as these require specialized equipment like log-periodic, biconical, and horn antennas to capture accurate electric field measurements in the far-field [29].

Exploring advanced shielding techniques, such as multilayer composite shields, could provide better EMI mitigation across a wider frequency range. Investigating different materials and configurations can help optimize shielding effectiveness while minimizing adverse effects like increased capacitance and resistance. Assessing the long-term performance and durability of shielded and unshielded cables under various operational conditions is also essential, including studying the effects of environmental factors, mechanical stresses, and ageing on EMI performance and cable integrity. Future studies should consider the integration of the analyzed cable systems with other aircraft systems to understand the cumulative impact of EMI. This holistic approach can help in designing more effective EMI mitigation strategies that account for interactions between different systems. As the aviation industry evolves, updating and expanding regulatory standards like DO-160 to encompass high-voltage electric propulsion systems is critical. Future work should focus on collaborating with regulatory bodies to develop comprehensive standards that address the unique challenges posed by electric aircraft.

Bibliography

[1] "Heart Aerospace AB," 2024. `https://heartaerospace.com/media-bank/`.

[2] F. Federal Aviation Administration, "FAA Projections Show Strong U.S. Air Travel Demand," 2020. `https://www.faa.gov/newsroom/faa-projections-show-strong-us-air-travel-demand`.

[3] J. Overton, "The Growth in Greenhouse Gas Emissions from Commercial Aviation," 2022.

[4] H. Maliska, "X-57 Maxwell Aircraft EMI/EMC Integration Lessons Learned," 2023.

[5] RTCA, "DO-160 - Environmental Conditions and Test Procedures for Airborne Equipment," 2023.

[6] R. R. Thakkar, "Electrical Equivalent Circuit Models of Lithium-ion Battery," 2021.

[7] J. Estaller, A. Kersten, M. Kuder, T. Thiringer, R. Eckerle, and T. Weyh, "Overview of battery impedance modeling including detailed state-of-the-art cylindrical 18650 lithium-ion battery cell comparisons," *Energies*, vol. 15, no. 10, p. 3822, 2022.

[8] M. Dong, L. Zhai, R. Gao, and X. Zhang, "Research on radiated electromagnetic interference (emi) from power cables of a three-phase inverter for electric vehicles," *ITEC Asia-Pacific*, 2014.

[9] C. F. Bohren and D. R. Huffman, *Absorption and Scattering of Light by Small Particles.* New York: Wiley-VCH, 1998.

[10] B. Ung and Y. Sheng, "Interference of surface waves in a metallic nanoslit," *Optics Express*, vol. 15, no. 19, pp. 1182–1187, 2007.

[11] A. D. Rakic, A. B. Djurisic, J. M. Elazar, and M. L. Majewski, "Optical properties of metallic films for vertical-cavity optoelectronic devices," *Applied Optics*, vol. 37, no. 22, pp. 5271–5283, 1998.

[12] A. Strikwerda, "Model cables and transmission lines in comsol multiphysics," 2024.

[13] J. D. Jackson, *Classical Electrodynamics.* Wiley, 1999.

[14] G. L. Pollack and D. R. Stump, *Electromagnetism.* Addison-Wesley, 2002.

[15] P. Musznicki, "Conducted emi propagation paths in dc-ac hard switching converter," *International Review of Electrical Engineering (IREE)*, vol. 8, no. 6, pp. 278–283, 2013. Gdansk University of Technology, Faculty of Electrical and Control Engineering, Poland.

[16] M. Steffka, "Conducted emissions and power supply filters," *IEEE EMC Society Central Texas Chapter*, 2011. IEEE EMCS Distinguished Lecturer.

[17] J.-S. L. S. C. X. Huang, E. Pepa and T. Nehl, “Three-phase inverter differential mode emi modeling and prediction in frequency domain,” *Industry Applications Conference, 2003. 38th IAS Annual Meeting. Conference Record of the*, vol. 3, pp. 2048–2055, 2003.

[18] C. Zhang, K. Li, S. Mcloone, and Z. Yang, “Battery modelling methods for electric vehicles - a review,” in *Proceedings of the European Control Conference (ECC)*, pp. 2673–2680, 2014.

[19] P. Mantzanas, D. Kuebrich, and T. Duerbaum, “Investigation of the dc-link capacitor current ripple in battery-fed pwm inverter systems,” in *2019 21st European Conference on Power Electronics and Applications (EPE ’19 ECCE Europe)*, 2019.

[20] A. Arif, Z. Wang, and J. Wang, “Load modeling – a review,” *IEEE Transactions on Smart Grid*, vol. 10, no. 3, pp. 2475–2485, 2019.

[21] C. T. for MATLAB and Simulink, “Motor speed: Simulink modeling,” 2022.

[22] J. Balcells, A. Santolaria, A. Orlandi, D. González, and J. Gago, “Emi reduction in switched power converters using frequency modulation techniques,” *IEEE Transactions on Electromagnetic Compatibility*, vol. 47, no. 3, pp. 569–576, 2005.

[23] A. Cordic and A. Wanitwijan, “Cable modelling for electric vehicle drivetrains,” 2021.

[24] J. Labus, “Measurement of resistance and impedances at high frequencies,” *Proceedings of the Institute of Radio Engineers*, vol. 19, no. 3, pp. 452–460, 1931.

[25] N. Idir, Y. Weens, and J.-J. Franchaud, “Skin effect and dielectric loss models of power cables,” *IEEE Transactions on Dielectrics and Electrical Insulation*, vol. 16, no. 1, pp. 147–154, 2009.

[26] J. G. Pazmany, D. Fodor, and B. Bäker, “Simulation of shield current in automotive high voltage systems,” *World Electr. Veh. J.*, vol. 12, no. 4, p. 217, 2021.

[27] H. Heydari, V. Abbasi, and F. Faghihi, “Impact of switching-induced electromagnetic interference on low-voltage cables in substations,” *IEEE Transactions on Electromagnetic Compatibility*, vol. 51, no. 4, pp. 937–944, 2009.

[28] EE Power, “Benefits of rugged dc-link capacitors in harsh applications,” *Technical Articles*, 2024.

[29] EMC FastPass, “Tem cell and gtem guide for radiated emissions & radiated immunity pre-compliance testing,” 2024. `https://emcfastpass.com/tem-cell-guide/`.

A

Appendix 1

A.1 Parameters for cable modelling

Table A.1: Parameters for unshielded cable to be used in Simulink model

Parameter	Notation	Value
Resistance of conductor	r_c	0.8878 mΩ
Inductance of cable	l_c	596.73 nH
Shunt capacitance of cable	c_c	16.343 pF

Table A.2: Parameters for shielded cable to be used in Simulink model

Parameter	Notation	Value
Resistance of conductor	r_c	1.0835 mΩ
Resistance of shield	r_s	0.9157 mΩ
Self-inductance of conductor	l_c	32.318 nH
Self-inductance of shield	l_s	5.4913 nH
Shunt capacitance of cable	c_c	1236 pF
Mutual inductance between conductor 1 & shield 1	M_{c1s1}	11.239 nH
Mutual inductance between conductor 1 & shield 2	M_{c1s2}	16.46 nH

DEPARTMENT OF ELECTRICAL ENGINEERING
CHALMERS UNIVERSITY OF TECHNOLOGY
Gothenburg, Sweden
www.chalmers.se

CHALMERS
UNIVERSITY OF TECHNOLOGY